International Journal of Solids and Structures 281 (2023) 112436

Contents lists available at ScienceDirect

International Journal of Solids and Structures

journal homepage: www.elsevier.com/locate/ijsolstr

Predicting transformation patterns in pseudoelastic NiTi tubes under proportional axial–torsion loading

Mohsen Rezaee-Hajidehi *, Stanisław Stupkiewicz

Institute of Fundamental Technological Research, Polish Academy of Sciences, Pawińskiego 5B, 02-106 Warsaw, Poland

ARTICLE INFO

Keywords:
Shape memory alloys
Phase transformation
Strain localization
Propagating instabilities
Finite-element method

ABSTRACT

We present a comprehensive modeling study on the patterns of propagating instabilities in NiTi tubes under proportional axial–torsion loading. Our study directly refers to the experimental work of Reedlunn et al. (2020), with a particular focus on the unique longitudinal transformation bands that occur in torsion-dominated loading paths. A previously-developed gradient-enhanced model of pseudoelasticity is employed and is adapted to incorporate the residual stresses. In addition, our finite-element setup accounts for the impact of collet grips on the NiTi tubes via a simplified frictional contact model. The results demonstrate the capability of the model in capturing subtle features of the transformation patterns observed in the experiment, including the multi-finger fronts in tension-dominated loading and longitudinal bands in torsion-dominated loading. Our study suggests that the combination of the residual stresses and the collet grips facilitates the formation of longitudinal bands.

1. Introduction

In polycrystalline shape memory alloys (SMAs), and particularly in textured NiTi, the stress-induced martensitic phase transformation may commence via deformation instability and formation of localized martensite bands. Subsequently, the transformation progresses through propagation of instabilities in the form of diffuse interfaces (macroscopic transformation fronts) that mediate the austenite (low-strained phase) and martensite (highly-strained phase) domains. It is now widely recognized that the occurrence of transformation instability in NiTi is attributed to the softening regime (a negative tangent modulus) in its intrinsic mechanical response, as supported by numerous theoretical studies (e.g., Ericksen, 1975; Abeyaratne and Knowles, 1993; Shaw and Kyriakides, 1997a). Experimentally, this was first demonstrated by Hallai and Kyriakides (2013) who successfully suppressed the instability of a NiTi strip (through lamination between two steel strips) under uniaxial tension and extracted the corresponding intrinsic response. Their findings were later corroborated by others (Alarcon et al., 2017; Watkins et al., 2018; Zhao et al., 2023; Greenly et al., 2023).

The earliest reports on transformation instabilities in NiTi can be traced back to the seminal works of Miyazaki et al. (1981a,b) and Shaw and Kyriakides (1995, 1997a,b) on NiTi wires and flat specimens subjected to uniaxial tension. The emergence of Lüders-like transformation bands and the accompanying stress plateau in the global mechanical response during both forward and reverse transformations were the primary and interesting observations of these investigations. Since then, a myriad of experimental studies have been conducted to characterize the transformation behavior of NiTi specimens under various experimental conditions. Of particular interest are the intriguing patterns of propagating instabilities observed in NiTi tubes, including helical bands and multi-finger fronts under uniaxial tension (Li and Sun, 2002; Feng and Sun, 2006; Bechle and Kyriakides, 2014; Reedlunn et al., 2014), diamond-shaped patterns under bending (Bechle and Kyriakides, 2014; Reedlunn et al., 2014), and inhomogeneous-to-homogeneous transitional patterning or complex mixed-mode patterns under combined loading conditions (Sun and Li, 2002; Bechle and Kyriakides, 2016; Reedlunn et al., 2020a).

One of the ambiguities in the transformation behavior of NiTi regards its response to shear. It has been the prevailing view that NiTi undergoes a homogeneous transformation under shear and shear-dominated loading. This was first demonstrated by Sun and Li (2002) who investigated the transformation morphology of NiTi tubes under combined non-proportional tension–torsion by using optical microscope. The authors have also found that the transformation mode gradually changes from localization to homogeneous as the loading alters from tension-dominated to shear-dominated. A homogeneous transformation in NiTi under shear-dominated loading was also affirmed by other experiments, either upon speculating it from a monotonic and smooth mechanical response (Orgéas and Favier, 1998), or by

* Corresponding author.
E-mail addresses: mrezaee@ippt.pan.pl (M. Rezaee-Hajidehi), sstupkie@ippt.pan.pl (S. Stupkiewicz).

https://doi.org/10.1016/j.ijsolstr.2023.112436
Received 13 March 2023; Received in revised form 25 June 2023; Accepted 20 July 2023
Available online 23 July 2023

analyzing the distribution of the strain fields across the specimen (Feng and Sun, 2007). In all these experiments, the global shear stress–shear strain response exhibited hardening, which is consistent with the homogeneous transformation mode.

In a more recent study, Reedlunn et al. (2020a) performed a comprehensive series of axial–torsion tests on NiTi tubes under isothermal conditions, and provided unprecedented visualization of the corresponding transformation patterns through the use of full-field Digital Image Correlation (DIC) measurements. Of exceptional interest was the observation of transformation localization in the form of longitudinal (almost parallel to the tube axis) transformation bands under torsion and torsion-dominated loading. Interestingly, despite the localized nature of the transformation, the global shear response remained monotonic and smooth, without any indication of localization effects, thus posing an apparent contradiction to the common consensus (note that the experimental setup employed by Reedlunn et al. (2020a) differs to some extent from that of Sun and Li (2002)). In addition to this, the observed pattern exhibited unique characteristics that further distinguish it from its rival pattern under tension, including a mild strain variation (2.8%–3.5%) between the low-strained and highly-strained domains and no propagation of the bands. Note that while the emergence of such distinctive longitudinal bands is unique to the experiment of Reedlunn et al. (2020a), similar inhomogeneous patterns of longitudinal bands have been reported in other experiments, including NiTi wires (Sedlák et al., 2021) and additively manufactured NiTi rods (Safaei et al., 2022) under torsion.

The experimental study of Reedlunn et al. (2020a) has provided a wealth of new data and valuable insights into the transformation behavior of NiTi SMA, and thereby, has opened up new avenues for further exploration through both modeling and experiment. In the light of this premise, the present work is devoted to the predictive modeling of the patterns of propagating instabilities in NiTi tubes under combined axial–torsion loading. Our primary focus is directed towards the tension–torsion quadrant. Additionally, a few compression–torsion loading paths are examined.

Our study places a special emphasis on the longitudinal bands and our endeavor is to provide a plausible explanation for their formation. Drawing upon the insights gained from the previous experiments (Reedlunn et al., 2020a; Sedlák et al., 2021; Safaei et al., 2022), it is possible to conclude that the longitudinal bands are definitely not experimental artifacts, rather they represent a genuine localized deformation mode. However, as argued by Reedlunn et al. (2020a), certain *extrinsic* factors may play a role in facilitating the formation of these bands. Here, we provide evidence in support of the hypothesis that residual stresses stored within the tube in conjunction with non-uniformity caused by the collets of the gripping setup might be these key extrinsic factors.

A phenomenological model of pseudoelasticity is employed in this study. The model has its origin in the non-gradient isothermal model developed by Stupkiewicz and Petryk (2013). In recent years, the gradient-enhanced version of this model has been successfully applied to simulate the patterns of propagating instabilities in NiTi specimens under uniaxial tension (Rezaee-Hajidehi and Stupkiewicz, 2018; Rezaee-Hajidehi et al., 2020) and NiTi tubes under combined non-proportional tension–torsion (Rezaee-Hajidehi and Stupkiewicz, 2021). To align with the specific aims of the present study, the gradient-enhanced model has been enriched with new features. Firstly, the eigenstrains arising from prior incompatible plastic deformation are incorporated into the kinematics, thus endowing the model to encompass residual stresses. An additional minor feature pertains to the austenite–martensite interaction energy which has been extended to account for the smoothness of the intrinsic mechanical response within the phase transformation initiation and saturation regions. Finally, in the finite-element simulations, to capture the effect of the collet grips on the NiTi tubes, we adopt a simple yet effective representation of tube–grip interaction through a frictional contact model.

2. Model formulation

A brief presentation of the model is provided in this section. The essential kinematic relations, the energy minimization problem, and the most important constitutive equations are described. The remaining model constituents are of secondary importance here, and thus their specification is relegated to appendices. For a more elaborate description of the model, the reader is referred to Rezaee-Hajidehi et al. (2020).

The model is developed within the finite-strain framework. The total deformation gradient $\boldsymbol{F} = \nabla\boldsymbol{\varphi}$, with $\boldsymbol{\varphi}$ as the mapping between the reference configuration and the current configuration, is multiplicatively decomposed into the elastic part $\boldsymbol{F}^{\mathrm{e}}$ and the inelastic part $\boldsymbol{F}^{\mathrm{in}}$,

$$\boldsymbol{F} = \boldsymbol{F}^{\mathrm{e}}\boldsymbol{F}^{\mathrm{in}}, \quad \boldsymbol{F}^{\mathrm{in}} = \boldsymbol{F}^{\mathrm{t}}\boldsymbol{F}^{0}, \tag{1}$$

where $\boldsymbol{F}^{\mathrm{t}}$ and $\boldsymbol{F}^{0}$ denote, respectively, the deformation gradient due to martensitic phase transformation and the deformation gradient associated with the residual stresses which typically arise during the material forming processes.[1] The specification of $\boldsymbol{F}^{0}$ is deferred to Appendix A.1.

The transformation deformation gradient $\boldsymbol{F}^{\mathrm{t}}$ is expressed as

$$\boldsymbol{F}^{\mathrm{t}} = \boldsymbol{R}^{\mathrm{t}}\boldsymbol{U}^{\mathrm{t}}, \tag{2}$$

where $\boldsymbol{U}^{\mathrm{t}}$ is the (symmetric) transformation stretch tensor and $\boldsymbol{R}^{\mathrm{t}}$ is a rotation tensor. Specifically, $\boldsymbol{R}^{\mathrm{t}} = \boldsymbol{I}$ is assumed, which leads to $\boldsymbol{F}^{\mathrm{t}} = \boldsymbol{U}^{\mathrm{t}}$. It is further assumed that $\boldsymbol{F}^{\mathrm{t}} = \boldsymbol{I}$ when the material is in the fully austenitic state. Moreover, martensitic phase transformation is considered to be an isochoric process, thus $\det\boldsymbol{F}^{\mathrm{t}} = \det\boldsymbol{U}^{\mathrm{t}} = 1$. The latter assumption is substantiated by the fact that SMAs typically exhibit an insignificant transformation volume change (Bhattacharya, 1992).

The transformation stretch tensor $\boldsymbol{U}^{\mathrm{t}}$ is postulated to be of the following form

$$\boldsymbol{U}^{\mathrm{t}} = \exp\boldsymbol{e}^{\mathrm{t}}, \quad \boldsymbol{e}^{\mathrm{t}} = \eta\bar{\boldsymbol{e}}^{\mathrm{t}}, \tag{3}$$

where $\boldsymbol{e}^{\mathrm{t}}$ represents the (logarithmic) transformation strain tensor, and $\exp(\cdot)$ denotes the tensor exponential. Here, $\boldsymbol{e}^{\mathrm{t}}$ is assumed to be deviatoric, $\operatorname{tr}\boldsymbol{e}^{\mathrm{t}} = 0$, hence it automatically ensures the incompressibility of the phase transformation, $\det\boldsymbol{U}^{\mathrm{t}} = 1$. In Eq. $(3)_2$, $\boldsymbol{e}^{\mathrm{t}}$ is defined in terms of the volume fraction of martensite η and the transformation strain of fully oriented martensite $\bar{\boldsymbol{e}}^{\mathrm{t}}$, which are subject to the following constraints,

$$0 \le \eta \le 1, \quad \bar{\boldsymbol{e}}^{\mathrm{t}} \in \bar{\mathcal{P}} = \{\bar{\boldsymbol{e}}^{\mathrm{t}} : \ g(\bar{\boldsymbol{e}}^{\mathrm{t}}) = 0\}. \tag{4}$$

Here, $\bar{\mathcal{P}}$ is the set of limit transformation strains characterized by the surface $g(\bar{\boldsymbol{e}}^{\mathrm{t}}) = 0$. In fact, the definition of the constitutive function $g(\bar{\boldsymbol{e}}^{\mathrm{t}})$ allows for a degree of flexibility. For the objectives of the present study, it is important that the function $g(\bar{\boldsymbol{e}}^{\mathrm{t}})$ is capable of taking into account the tension–compression asymmetry and the transverse isotropy, see the detailed discussion in Rezaee-Hajidehi and Stupkiewicz (2021). With a slight modification of the original formulation developed by Sadjadpour and Bhattacharya (2007), the function $g(\bar{\boldsymbol{e}}^{\mathrm{t}})$ is adopted here as (Stupkiewicz and Petryk, 2013)

$$g(\bar{\boldsymbol{e}}^{\mathrm{t}}) = \left[(-I_2)^{3/2} - bI_3 - cI_4^3\right]^{1/3} - a, \tag{5}$$

where I_2 and I_3 are the principal invariants of the transformation strain tensor $\bar{\boldsymbol{e}}^{\mathrm{t}}$ and I_4 is a mixed invariant, i.e.,

$$I_2 = -\frac{1}{2}\operatorname{tr}(\bar{\boldsymbol{e}}^{\mathrm{t}})^2, \quad I_3 = \det\bar{\boldsymbol{e}}^{\mathrm{t}}, \quad I_4 = \boldsymbol{m}\cdot\bar{\boldsymbol{e}}^{\mathrm{t}}\boldsymbol{m}, \tag{6}$$

with $\boldsymbol{m}$ as the axis of the transverse isotropy. Recall that $\bar{\boldsymbol{e}}^{\mathrm{t}}$ is deviatoric, thus $I_1 = \operatorname{tr}(\bar{\boldsymbol{e}}^{\mathrm{t}}) = 0$. The parameters a, b and c in Eq. (5) characterize

[1] The cold-drawing process of the tube entails a number of stages that can induce inhomogeneous (and incompatible) deformation (of mechanical or thermal origin), and thus may lead to the development of residual stresses.

the shape and size of the $g(\bar{\boldsymbol{e}}^{\mathrm{t}})=0$ surface and are defined in terms of the maximum tensile and compressive transformation strains along the $\boldsymbol{m}$ axis, ϵ_{T} and ϵ_{C} respectively, and perpendicular to the $\boldsymbol{m}$ axis, $\epsilon_{\mathrm{T}}^{\star}$ and $\epsilon_{\mathrm{C}}^{\star}$ respectively, in the following forms,

$$a=\epsilon_{\mathrm{T}}\Big[\frac{3\sqrt{3}}{4(1+\alpha^3)}\Big]^{1/3},\quad b=\frac{\sqrt{3}}{6}\frac{9\alpha^3\beta^3-7\alpha^3+7\beta^3-9}{(1+\alpha^3)(1+\beta^3)},$$
$$c=\frac{2\sqrt{3}}{3}\frac{\alpha^3-\beta^3}{(1+\alpha^3)(1+\beta^3)}, \tag{7}$$

where $\alpha=\epsilon_{\mathrm{T}}/\epsilon_{\mathrm{C}}$ and $\beta=\epsilon_{\mathrm{T}}^{\star}/\epsilon_{\mathrm{C}}^{\star}$ control the degree of tension–compression asymmetry along $\boldsymbol{m}$ and perpendicular to $\boldsymbol{m}$, respectively. An isotropic material is described by $\alpha=\beta$ and a transversely isotropic material by $\alpha\neq\beta$, where the deviation of β from α quantifies the degree of transverse isotropy.

Note that, in our finite-element simulations, we consider transversely isotropic NiTi material, with the axis of transverse isotropy $\boldsymbol{m}$ directed along the tube axis. This choice is in line with the common feature of drawn NiTi tubes (and also NiTi wires) that exhibit a strong ⟨111⟩ fiber texture along the tube axis, which is also observed for the NiTi tubes investigated by Reedlunn et al. (2020a), see their Fig. 2.

Our constitutive model relies upon two main elements, namely the Helmholtz free energy function and the dissipation potential. Assuming isothermal conditions (the thermomechanical coupling is discussed in Appendix C), the total Helmholtz free energy $\boldsymbol{\Phi}$ is defined as the sum of the chemical energy ϕ_0, the elastic strain energy ϕ_{el}, the interaction energy ϕ_{int} and the gradient energy ϕ_{grad} components integrated over the entire body B,

$$\boldsymbol{\Phi}=\int_B \phi\,\mathrm{d}V,\quad \phi(\boldsymbol{F},\bar{\boldsymbol{e}}^{\mathrm{t}},\eta,\nabla\eta)=\phi_0(\eta)+\phi_{\mathrm{el}}(\boldsymbol{F},\bar{\boldsymbol{e}}^{\mathrm{t}},\eta)+\phi_{\mathrm{int}}(\bar{\boldsymbol{e}}^{\mathrm{t}},\eta)+\phi_{\mathrm{grad}}(\nabla\eta). \tag{8}$$

At the same time, a rate-independent dissipation potential is considered and is adopted in the following incremental form,

$$\Delta D=\int_B \Delta D\,\mathrm{d}V,\quad \Delta D(\Delta\eta)=f_{\mathrm{c}}|\Delta\eta|, \tag{9}$$

where f_{c} is a material parameter characterizing the width of the hysteresis loop in the intrinsic stress–strain response, and $\Delta\eta=\eta-\eta_n$, with η_n as the martensite volume fraction at the previous time step.

Having the Helmholtz free energy functional $\boldsymbol{\Phi}$ and the global dissipation potential ΔD at hand, the evolution of the unknown fields $\boldsymbol{\varphi}$, $\bar{\boldsymbol{e}}^{\mathrm{t}}$ and η is governed by the incremental energy minimization principle (e.g. Petryk, 2003; Stupkiewicz and Petryk, 2013; Rezaee-Hajidehi and Stupkiewicz, 2018),

$$\Pi=\Delta\boldsymbol{\Phi}+\Delta\Omega+\Delta D\ \rightarrow\ \min_{\boldsymbol{\varphi},\bar{\boldsymbol{e}}^{\mathrm{t}},\eta} \tag{10}$$

subject to the constraints on the martensite volume fraction η and limit transformation strain $\bar{\boldsymbol{e}}^{\mathrm{t}}$ given in Eq. (4). The term $\Delta\Omega$ in the expression for Π represents the increment of the potential energy of the external loads, which are considered as conservative. Actually, in our finite-element simulations, the external load is modeled through the frictional contact interaction between the collet grips and the NiTi tube, see the details in Section 3.1. Thereby, $\Delta\Omega=0$, while the respective details of the formulation are omitted for simplicity.

Next, we elaborate on the Helmholtz free energy function ϕ. Among the components of ϕ, only the interaction energy ϕ_{int}, in its specific form (11), is new in comparison with the earlier versions of the model (Stupkiewicz and Petryk, 2013; Rezaee-Hajidehi and Stupkiewicz, 2018; Rezaee-Hajidehi et al., 2020), and thus is discussed here. On the other hand, the chemical energy ϕ_0, the elastic strain energy ϕ_{el} and the gradient energy ϕ_{grad} are rather standard and the respective details are laid out in Appendix A.2.

The new interaction energy ϕ_{int} delivers a nonlinear intrinsic stress–strain response by accounting for a smooth transition within the transformation-onset and transformation-saturation regions, representing an inherent feature of NiTi that has been clearly observed in the experiments (e.g. Daly et al., 2007; Hallai and Kyriakides, 2013; Alarcon et al., 2017) and has been predicted by micromechanical analyses (e.g. Thamburaja and Anand, 2001; Stupkiewicz and Petryk, 2010). In general, the incorporation of a nonlinear intrinsic response into the phenomenological description is realized via tailoring the interaction energy either based on the empirical macroscopic relations (e.g. Lagoudas et al., 2012; Wang et al., 2017) or on account of the micromechanical considerations (Peultier et al., 2006; Kelly et al., 2016; Frost et al., 2021; Stupkiewicz et al., 2021). In the present model, the former approach is used, as elaborated below.

The interaction energy ϕ_{int} is adopted in the form

$$\phi_{\mathrm{int}}(\bar{\boldsymbol{e}}^{\mathrm{t}},\eta)=\frac{1}{2}H(\bar{\boldsymbol{e}}^{\mathrm{t}})\eta^2+h(\eta). \tag{11}$$

Here, the first term on the right-hand side specifies the type of the intrinsic stress–strain response within the transformation regime, i.e., softening- or hardening-type according to the sign of the interaction coefficient $H(\bar{\boldsymbol{e}}^{\mathrm{t}})$. The coefficient $H(\bar{\boldsymbol{e}}^{\mathrm{t}})$ is formulated in terms of the transformation strain $\bar{\boldsymbol{e}}^{\mathrm{t}}$ in the following form (Rezaee-Hajidehi et al., 2020)

$$H(\bar{\boldsymbol{e}}^{\mathrm{t}})=H_{\mathrm{T}}-\frac{(\epsilon_{\mathrm{T}}-\epsilon(\bar{\boldsymbol{e}}^{\mathrm{t}}))(H_{\mathrm{T}}-H_{\mathrm{C}})}{\epsilon_{\mathrm{T}}-\epsilon_{\mathrm{C}}}, \tag{12}$$

where $\epsilon(\bar{\boldsymbol{e}}^{\mathrm{t}})=\sqrt{\frac{2}{3}\,\mathrm{tr}(\bar{\boldsymbol{e}}^{\mathrm{t}})^2}$ denotes the equivalent transformation strain, H_{T} denotes the softening/hardening modulus that corresponds to uniaxial tension, i.e., when $\epsilon(\bar{\boldsymbol{e}}^{\mathrm{t}})=\epsilon_{\mathrm{T}}$, and H_{C} denotes the softening/hardening modulus that corresponds to uniaxial compression, i.e., when $\epsilon(\bar{\boldsymbol{e}}^{\mathrm{t}})=\epsilon_{\mathrm{C}}$. Typically, a softening-type response is adopted for tension (i.e., with $H_{\mathrm{T}}<0$) and a hardening-type response is adopted for compression (i.e., with $H_{\mathrm{C}}>0$).

Note that, according to the model, the response in shear depends on both H_{T} and H_{C}, but also varies in line with the degree of transverse isotropy of the material, as discussed in Rezaee-Hajidehi and Stupkiewicz (2021). The degree of transverse isotropy is determined by parameter β in the limit transformation strain function $g(\bar{\boldsymbol{e}}^{\mathrm{t}})$, cf. Eq. (5). For a strongly transversely isotropic material, the response in shear results from a balance between the softening-type response in tension and the hardening-type response in compression. As the material tends to be isotropic, the response in shear tends to follow the softening-type response in tension. In any case, the transformation-onset stress in shear weakly depends on β and lies roughly in the middle between those in tension and compression (when expressed in terms of the equivalent von Mises stress).

The term $h(\eta)$ on the right-hand side of Eq. (11) is responsible for the nonlinearity in the intrinsic stress–strain response. In fact, $h(\eta)$ influences the constitutive response only through its derivative $h'(\eta)$. Thus, only $h'(\eta)$ is needed to be specified. Following the work of Wang et al. (2017), a tangent-based function is adopted for $h'(\eta)$ in the form

$$h'(\eta)=a_1\tan\Big(\frac{\pi}{2}(\eta-a_2)\Big)^{a_3}, \tag{13}$$

where the parameters $0<a_1$, $0<a_2<1$ and a_3 (a non-negative integer) control, respectively, the stress level, the extent, and the degree of nonlinearity associated with the transformation-onset and transformation-saturation smooth transitions.

Fig. 1 depicts the intrinsic stress–strain response generated by the model under the loading conditions of uniaxial tension, uniaxial compression and shear. The responses are shown for the cases with and without the contribution of $h(\eta)$. In the latter case, a trilinear response with abrupt transitions is obtained. Material parameters correspond here to those specified in Table E.1 and used in Section 3 (the effect of parameter β on the softening/hardening response in shear is discussed in Section 3.4, see Fig. 10(b)).

The implementation of the present model in the finite-element framework relies on the micromorphic regularization approach which follows Rezaee-Hajidehi and Stupkiewicz (2018), see also Mazière and

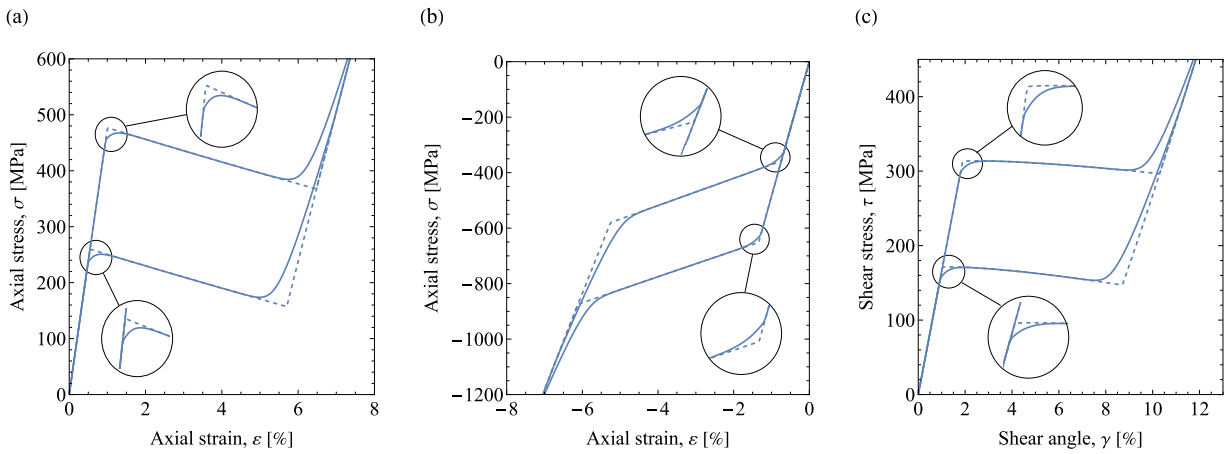

Fig. 1. The intrinsic stress–strain response corresponding to (a) uniaxial tension, (b) uniaxial compression, and (c) shear (material parameters correspond to those specified in Table E.1). The dashed curves indicate the trilinear response obtained by excluding the contribution of $h(\eta)$, see Eqs. (11) and (13). Within the transformation-saturation region, the model with $h(\eta)$ exhibits a very gradual transition with a stress–strain slope that tends to the apparent elastic modulus of martensite.

Forest (2015). Details of the micromorphic regularization of the model are provided in Appendix B. Despite the nearly isothermal conditions in the numerical studies reported in Section 3, the actual model employed is thermomechanically coupled. The thermomechanical coupling effects offer a natural regularization to the problem at hand, and render the computational model more robust. The constitutive equations describing the thermomechanical coupling are outlined in Appendix C. Moreover, further technical details concerning the finite-element treatment are given in Appendix D.

3. Simulations: setup, results and discussion

This section is devoted to the analysis of NiTi tubes under proportional axial–torsion loading. Our modeling scenario is built upon the experiment of Reedlunn et al. (2020a), and throughout the analysis, direct comparisons are made between the simulation and experimental results. Accordingly, in the interest of consistency, we strive to adopt the same notations and terminologies as in Reedlunn et al. (2020a). The problem setup and modeling considerations are given in Section 3.1, while the identification of the material parameters is discussed in Section 3.2. To serve as a baseline, we first present in Section 3.3 the simulation results for a NiTi tube subjected to uniaxial tension. Subsequently, in Section 3.4, the results related to simple torsion are discussed, with a particular focus on longitudinal phase transformation bands. The simulation results of tension–torsion and compression–torsion are discussed in Sections 3.5 and 3.6, respectively.

3.1. Problem description

The setup of the problem is depicted in Fig. 2. The geometry of the tube follows that in the experiment (Reedlunn et al., 2020a). The tube has an outer diameter of $D_0 = 3.18$ mm, a wall thickness of $H_0 = D_0/10 = 0.318$ mm, and a free (ungripped) length L_0 that ranges between 7.19 mm and 20.81 mm, as reported in Fig. 2(c). In the experiment, the load is transmitted from the loading frame to the tube specimen via collets (3.5 mm ER-16 steel collets) that grip the tube at both ends. The collets have 6 slots and a maximum clamping diameter of 3.5 mm. To simulate the loading configuration of the experiment, the load is here applied at the 'gripped' segments of the tube through frictional contact. The collet slots are resembled, as shown in the inset in Fig. 2(a), by splitting the contact surface (assumed rigid) into 6 sub-surfaces with an intermediate angular gap of approximately 13°, which is estimated based on the perimeter of the tube cross-section and the collet clamping range of 2.5–3.5 mm. Such a simplified contact representation allows to account for grip slippage that occurs inevitably in the experiment and provides, by construction, a natural trigger to the nucleation of the phase transformation. A contact model with Tresca-type friction is employed, in which the limit friction stress T_c is independent of the normal pressure and, for simplicity, bilateral contact conditions are imposed in the normal direction. Details regarding the finite-element implementation of the contact model are given in Appendix D. It is important to note that in the majority of our simulations, the radial compression imposed by the collets is neglected.

The loading is exerted in a displacement-control mode by prescribing extension δ and twist angle φ directly at the top collet slots, whereas the axial displacement and rotation of the bottom collet slots are constrained to be zero. In doing so, the compliance of the loading device is neglected. The proportional axial–twist loading is parametrized by the strain-path angle[2] ω calculated as

$$\tan\omega = \frac{\gamma_{\text{grip}}}{\varepsilon_{\text{grip}}}, \quad \gamma_{\text{grip}} = \frac{\varphi D_0}{2L_0}, \quad \varepsilon_{\text{grip}} = \frac{\delta}{L_0}, \tag{14}$$

where $\varepsilon_{\text{grip}}$ represents the overall (engineering) axial strain and γ_{grip} represents the overall shear strain (referred to as 'grip axial strain' and 'grip shear strain' in the sequel). The total number of 12 strain paths, among those reported by Reedlunn et al. (2020a), are considered in this study, see Fig. 2(b,c). This list includes uniaxial tension ($\omega = 0°$), simple torsion ($\omega = 90°$), 7 tension–torsion paths ($0° < \omega < 90°$), and 3 compression–torsion paths ($90° < \omega < 180°$), each corresponding to a complete loading–unloading cycle. Note that, due to the occurrence of buckling at high compressive stresses, the analysis of the compression–torsion loading paths is limited to only three cases with relatively low-to-moderate compressive stresses. Further details on this matter are provided in Section 3.6.

In all loading cases, a constant loading rate (both the grip axial strain rate $\dot{\varepsilon}_{\text{grip}}$ and the grip shear strain rate $\dot{\gamma}_{\text{grip}}$) of 10^{-5} s^{-1} is adopted, which is of the same order as those used in the experiment, and is low enough to ensure nearly isothermal conditions. The conductive heat exchange between the tube and the grips is accounted for by fixing the temperature of the collet slots to the ambient temperature $T_0 = 23$ °C. At the same time, the convective heat exchange between the tube free surface and the ambient is neglected, as it makes a negligible contribution in the present analysis (He and Sun, 2010).

[2] Note that, for consistency with the presentation of the results in the subsequent sections, the strain-path angle ω is here defined in terms of the shear strain γ_{grip}, and not in terms of the *tensorial* shear strain $\gamma_{\text{grip}}/2$ as in Reedlunn et al. (2020a). Accordingly, ω differs from the angle η defined by Reedlunn et al. (2020a).

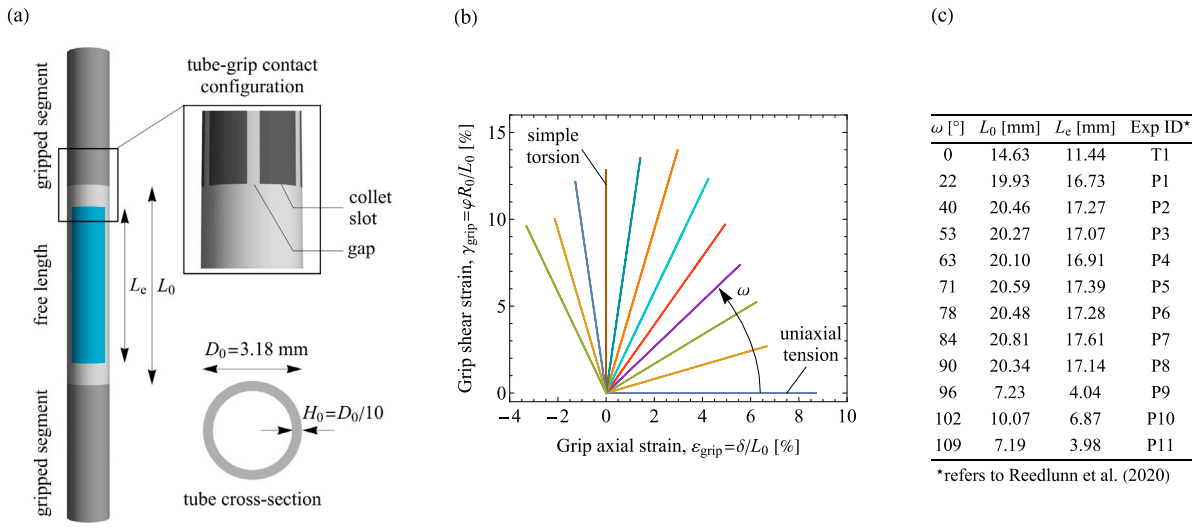

ω [°]	L_0 [mm]	L_e [mm]	Exp ID*
0	14.63	11.44	T1
22	19.93	16.73	P1
40	20.46	17.27	P2
53	20.27	17.07	P3
63	20.10	16.91	P4
71	20.59	17.39	P5
78	20.48	17.28	P6
84	20.81	17.61	P7
90	20.34	17.14	P8
96	7.23	4.04	P9
102	10.07	6.87	P10
109	7.19	3.98	P11

*refers to Reedlunn et al. (2020)

Fig. 2. Setup of the problem: (a) tube geometry and the gripping layout, (b) the proportional axial–shear strain paths selected for the simulations, and (c) geometric and loading parameters of each simulation and the corresponding experiment from Reedlunn et al. (2020a). The blue-shaded area in panel (a) represents a section of the tube (with an axial length L_e and an angular extent of 100°) that resembles the virtual DIC extensometer region in the experiment.

The analysis of the simulation results in the subsequent sections is focused mainly on the transformation pattern and global mechanical response, and their comparison with the experimental data of Reedlunn et al. (2020a). The experimental results of full-field DIC measurements are reported in terms of a co-rotated strain measure, which we are not able to uniquely reproduce. Therefore, the predicted transformation patterns are represented by the spatial distribution of the components of the Green–Lagrange strain measure, in particular, the axial strain ε_{ZZ} and shear strain $\gamma_{\Theta Z}$ components. To make the comparison of the transformation patterns more accurate, the color maps used to display the axial and shear strains are the same as those used by Reedlunn et al. (2020a). The mechanical responses are, in general, reported in terms of nominal (engineering) stresses versus grip strains. However, some comparisons are also made with the responses based on the average strains $\bar{\varepsilon}_{ZZ}$ and $\bar{\gamma}_{\Theta Z}$, which are calculated from the average axial displacement and average rotation of the tube at the ends of the 'virtual extensometer' region, see the blue-shaded area in Fig. 2(a). Note that our way of calculating the average strains is not entirely consistent with that in the experiment which was based on the spatial averaging of the strain fields over a 100°-wide virtual extensometer region on the tube surface.

The nominal axial stress σ and the nominal shear stress τ are computed as $\sigma = P/A_0$ and $\tau = MD_0/(2J_0)$, where P and M denote, respectively, the axial force and the torque, and A_0 and J_0 denote, respectively, the initial cross-section area and the initial polar moment of inertia. To be consistent with the experiment, the loading in each simulation is applied until the stress radius in the axial–shear stress space, i.e., $\sqrt{\sigma^2+\tau^2}$, reaches the maximum stress radius in the analogous experiment, and subsequently unloading begins. In compression–torsion cases, however, in order to avoid buckling of the tube, the loading is stopped at a somewhat smaller stress radius.

An important parameter that needs to be appropriately specified is the limit friction stress T_c associated with the tube–grip contact interaction. The parameter T_c is calibrated by using the experimental mechanical responses based on the grip measurements. From our preliminary analysis it turned out that a single friction stress T_c does not lead to satisfactory predictions in all simulations. Accordingly, T_c ought to be calibrated separately for the different loading combinations analyzed. From the experimental viewpoint, it is well-known that the strains derived from grip motion are prone to various experimental artifacts, such as those caused by unavoidable grip slippage or excessive clamping forces (Churchill et al., 2009; Reedlunn et al., 2020a). The gripping artifacts are also discernible in the results of Reedlunn et al. (2020a), see the corresponding supplemental material (Reedlunn et al., 2020b), and the associated uncertainties are clearly reflected in the mechanical responses (in terms of grip strains) of repeated experiments (compare, e.g., T1 and T3 or P2 and P2m) which exhibit roughly the same maximum global stress but fairly different final remnant grip strains. In our rudimentary representation of the collet–tube interaction, the only viable way to account for gripping artifacts is by adjusting the parameter T_c. This aspect is elaborated later on.

3.2. Identification of material parameters

The material parameters that characterize the intrinsic stress–strain response of NiTi are selected on the basis of the following main considerations. (i) The intrinsic response in uniaxial tension is tuned such that the corresponding Maxwell construction (e.g., Stupkiewicz et al., 2021) matches with a reasonable accuracy the global response (in terms of gage strains) of the NiTi tube in the experiment, in particular, in relation to the level of stress plateau, the transformation strain, and the width of the hysteresis loop. (ii) The tension–compression asymmetry (controlled by parameter α, cf. Eq. (5)) and the hardening modulus H_C, see Eq. (12), are adopted to represent the hardening-type response under uniaxial compression, see Fig. 3(b) and the discussion below. (iii) The degree of transverse isotropy (controlled by parameter β, cf. Eq. (5)) is selected so that the intrinsic response in shear exhibits a relatively weak softening within the transformation regime, see also the related discussion in Rezaee-Hajidehi and Stupkiewicz (2021). As will be shown in Section 3.4, the transformation pattern and the mechanical response of the NiTi tube under torsion are highly sensitive to the choice of parameter β. All the material parameters are specified in Appendix E, and the resulting characteristic intrinsic responses are depicted in Fig. 1, see also Fig. 3.

While some material parameters can be determined with a high level of confidence, there exist parameters that have some uncertainty. This, in particular, concerns the softening modulus in tension, H_T, which cannot be measured directly in the experiment unless special techniques are employed (Hallai and Kyriakides, 2013; Alarcon et al., 2017; Zhao et al., 2023; Greenly et al., 2023). Such a detailed characterization is not available for the material under investigation (in fact, as documented in Watkins et al. (2018), an attempt was made to measure

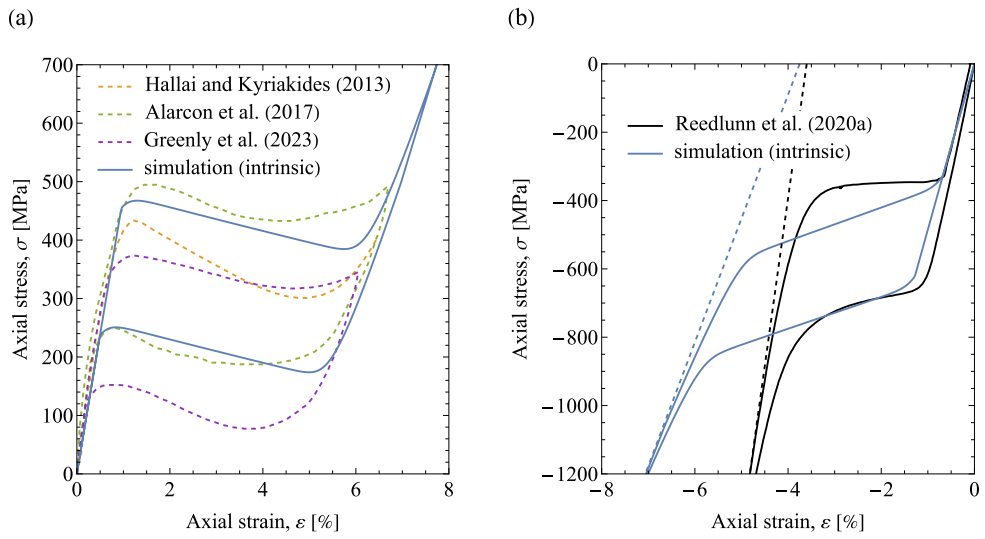

Fig. 3. Comparison between the calibrated *intrinsic* response in tension (a) and compression (b) with the NiTi responses obtained from experiments. The dashed curves in panel (a) refer to the experimentally-determined intrinsic responses (note that only the loading stage is reported by Hallai and Kyriakides (2013)). The dashed lines in panel (b) indicate the stress-free transformation strains.

the intrinsic response of the Reedlunn et al. (2020a) NiTi tubes using the approach of Hallai and Kyriakides (2013), but it was not successful), and therefore, only a rough estimate of H_T could be adopted. Fig. 3(a) shows that our calibrated intrinsic response in tension exhibits a realistic level of softening compared to the available experimental intrinsic responses obtained for NiTi (the level of transformation stress is not a subject of comparison, as it depends on many factors, for instance, on the temperature).

The response in compression exhibits a hardening behavior, thus allowing for a more confident identification of the hardening modulus H_C compared to H_T. Fig. 3(b) depicts the calibrated intrinsic response in compression and compares it with the experimental one (case C2) of Reedlunn et al. (2020a). Although there is a noticeable difference between the two responses, it mainly stems from the disparity in the elastic moduli of martensite (since our focus is mainly towards the tension–torsion quadrant, the elastic shear and bulk moduli are adopted in favor of a more accurate representation of the apparent elastic response in tension rather than in compression, see the related discussion in Appendix A.2). At the same time, important features such as the transformation-onset stress, the transformation strain (both governed by parameter α), and the hysteresis loop area are represented reasonably well. Reedlunn et al. (2020a) discussed that the elastic stiffness of martensite induced by compression is higher compared to tension (besides, the apparent modulus of austenite shows a dependence on load direction, which is attributed to the intermediate R-phase transformation induced under tension), while in our model the elastic moduli do not vary with the loading direction. Consequently, the compressive response cannot be accurately represented by our model, and this introduces some ambiguity in selecting H_C.

As reported by Reedlunn et al. (2020a), during the examination of the crystallographic features, it was observed that the quarter-ring NiTi specimens (of the length of 155 mm) bent radially inward and formed a curvature of 740 ± 100 mm radius in the axial–radial plane to relieve the residual stresses. In line with this experimental evidence, the radial and axial strain parameters associated with the residual stresses, i.e., ϵ_R and ϵ_Z, see the description of $\boldsymbol{F}^0$ in Appendix A.1, are taken such that their mutual interaction yields nearly the same curvature in the same material configuration as in the experiment. The strain parameters are identified as $\epsilon_R = -1\%$ and $\epsilon_Z = -0.45\%$, see Appendix A.1. The crucial role of the residual stresses on the formation of longitudinal bands under torsion is demonstrated in Section 3.4. It should be remarked that while the target curvature can be attained by various combinations of radial strain ϵ_R and axial strain ϵ_Z, a suitable combination that promotes the formation of longitudinal phase transformation bands has been selected. Nevertheless, the resulting residual stresses in the full-tube configuration may not fully align with the residual stresses present in real tubes, which are not known.

3.3. NiTi tube under uniaxial tension

Fig. 4 depicts the predicted transformation pattern and the mechanical response for the tube under uniaxial tension ($\omega = 0°$) along with the comparisons with the experimental results (case T1). The simulation snapshots have been selected in such a way that the corresponding points on σ–ϵ_{grip} response (denoted by markers) match those from the experiment, and the view point of the snapshots has been adjusted to align with the experimental one. The horizontal solid and dotted lines superimposed on the simulation snapshots indicate, respectively, the calculation region of average strains (i.e., the ends of the virtual extensometer region, as analogously shown by the horizontal line in the experimental snapshots) and the intersection between the free and gripped segments of the tube. Concerning the mechanical response, both the response based on the grip axial strain ϵ_{grip} and the response based on the average axial strain $\bar{\epsilon}_{ZZ}$ are presented to illustrate the underlying differences between the two responses. A limit friction stress of $T_c = 5$ MPa is adopted for this simulation.

As shown in Fig. 4(a), the predicted transformation pattern bears a striking resemblance to the experimental one. The transformation begins with the nucleation of martensite bands, in the shape of fingers (or prongs), at both lower and upper grips, and then proceeds with the propagation of the lower macroscopic front, while the upper fingers are halted. Note that no artificial imperfection has been introduced to favor the lower transformation front, and the observed asymmetry is a result of numerical imperfections. The evolving front has a typical criss-cross pattern (Shaw and Kyriakides, 1997b; Reedlunn et al., 2014; Shariat et al., 2022) featuring right-handed and left-handed fingers that emerge at the sides of the tube (not visible in the snapshots) and wind towards each other in a symmetric manner, and merge at the front (in the simulation snapshots, the view point has been adjusted such that fingers merge in the same region as in the experimental snapshots) and at the back. Both the right-handed and left-handed fingers are characterized by the trailing-edge angle $\alpha_1 = 53°$ and the leading-edge angle $\alpha_2 = 63°$ with respect to the tube axis, see Fig. 5. These angles remain relatively constant throughout the evolution. At a later stage, when the front gets

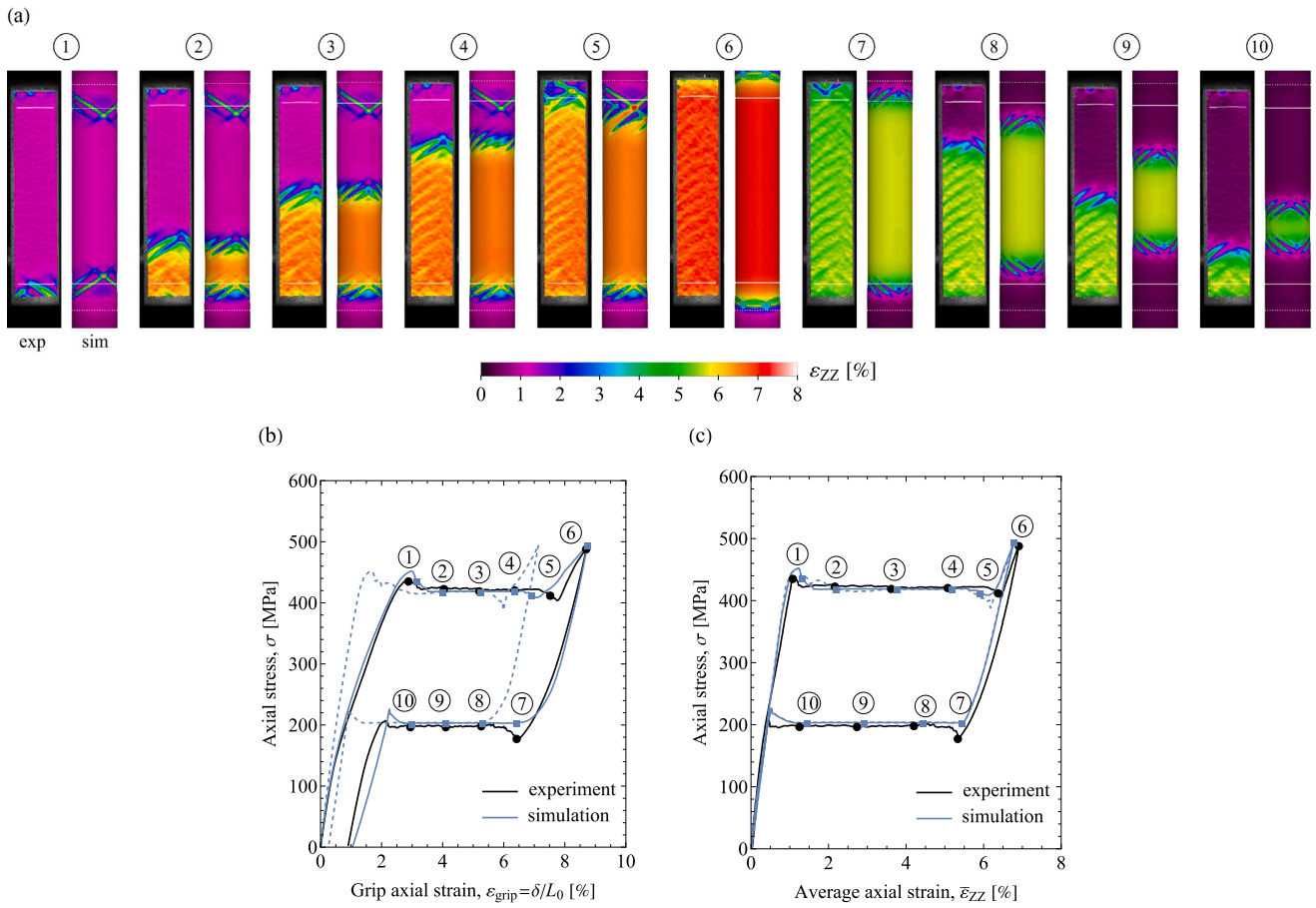

Fig. 4. Simulation results for the case of uniaxial tension ($\omega = 0°$) and their comparison with the experimental results (case T1) of Reedlunn et al. (2020a): (a) snapshots of the axial strain field ε_{ZZ}, (b,c) the global mechanical response represented in terms of (b) axial stress–grip axial strain (σ–ε_{grip}), and (c) axial stress–average axial strain (σ–$\bar{\varepsilon}_{ZZ}$). The left-hand and right-hand snapshots in panel (a) correspond, respectively, to the experiment (reproduced with permission from Elsevier) and simulation. The dashed curves in panels (b,c) represent the response for the case with the limit friction stress of $T_c = 20$ MPa, while the corresponding transformation pattern is shown in Fig. 6.

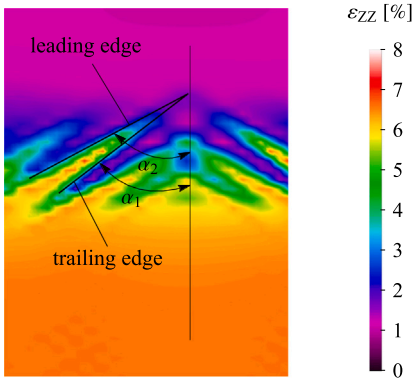

Fig. 5. A close-up view of the propagating front in uniaxial tension (shown in the undeformed and unwrapped-tube configuration).

sufficiently close to the upper fingers, they merge, as seen in snapshot '5', and subsequently, upon further loading, the diffuse ring-like fronts protrude into the gripped segments. During unloading, the macroscopic front maintains the same pattern as in loading, however, this time, both lower and upper fronts shrink concurrently, though not in an entirely symmetric fashion, and thus, in this sense, the predicted pattern differs from the experimental one where only one reverse transformation front is active. Throughout the process, the same transformation pattern is replicated at the back of the tube.

There are some other noteworthy differences between the predicted and experimental transformation patterns. In the experiment, the right-handed and left-handed fingers do not grow symmetrically; rather, they grow in an alternating manner. Also, the angles at which these fingers grow change by about 2°–4° during the evolution. This asymmetric nature of the transformation is likely attributed to the imperfections (such as geometric imperfections or microstructure impurities) that always exist in practice and result in the deviation from the ideal symmetric transformation patterning. Another difference is related to the striations left behind by the transformation front. While these striations are clearly visible in the experimental pattern, as also seen in the experiments involving NiTi strip or dogbone specimens (e.g., Shaw and Kyriakides, 1997b; Shariat et al., 2022), they are hardly visible in the predicted pattern. According to Reedlunn et al. (2020a), the striations are domains of incompletely-transformed martensite, which can transform further as the tube enters the final stiffening stress–strain stage, as can be inferred from the comparison between the experimental snapshots '5' and '6'. In the present model, the intrinsic stress–strain response is characterized by a gradual nonlinear stiffening within the transformation saturation region, see Fig. 1, which results in an incomplete transformation during loading. However, it seems that this feature alone is insufficient to fully capture the striations observed in the experiment. The martensite reorientation mechanism at the propagating front is another important factor that should be considered. Specifically, the local transformation strain evolution within the fingers differs from that within the surrounding domains, leading to distinct

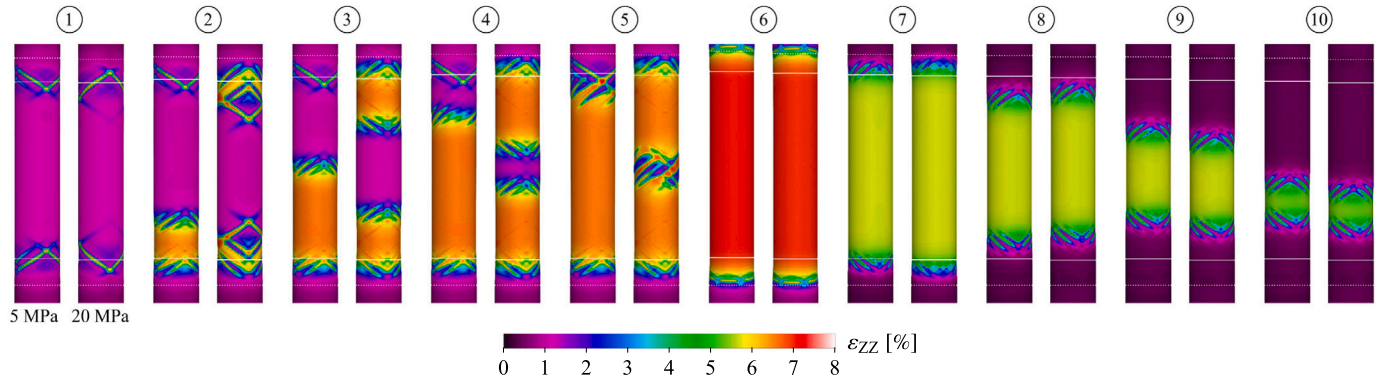

Fig. 6. Transformation pattern for the case of uniaxial tension ($\omega = 0°$) with a limit friction stress of $T_c = 20$ MPa and its comparison with that of the reference simulation with $T_c = 5$ MPa. The snapshots are taken at approximately the same average axial strain $\bar{\varepsilon}_{ZZ}$, see Fig. 4(c).

evolution pathways, and hence striations. As such, to accurately model the striations, it would be necessary to adopt a more sophisticated description of martensite reorientation mechanism, for instance, by enhancing the dissipation potential to account for the energetic cost of the evolution of the transformation strain $\bar{e}^t$.

We now describe the mechanical response of the tube, as depicted in Fig. 4(b,c), by highlighting the most important aspects. Like the transformation pattern, the predicted mechanical response is also in a strong agreement with the experimental one. The nonlinear behavior in the early and late stages of loading and unloading and the final remnant strain (of about $\varepsilon_{grip} = 1\%$) caused by the grip slippage are correctly captured in the simulation. The sharp stress changes linked to specific transformation events, such as the band nucleation and the martensite domain merger, are also well reproduced, except the sudden stress rise associated with the initiation of the reverse transformation during unloading. In contrast to the σ–ε_{grip} response, the σ–$\bar{\varepsilon}_{ZZ}$ response is almost linear in the early and late stages, despite some minor nonlinearity in the experimental response (recall that R-phase transformation is not incorporated in the present model), and shows no sign of remnant deformation.

Fig. 4(b,c) also illustrates the mechanical response obtained for a higher limit friction stress of $T_c = 20$ MPa, see the dashed curves. The σ–ε_{grip} responses obtained for $T_c = 5$ MPa and $T_c = 20$ MPa are markedly different, in particular the final remnant strain is much smaller for $T_c = 20$ MPa, as a result of reduced grip slippage. At the same time, the corresponding σ–$\bar{\varepsilon}_{ZZ}$ responses are very similar. This highlights the well-recognized importance of the gage response in diminishing the experimental artifacts caused by the grip slippage. Note also that, as shown in Fig. 6, the transformation patterns obtained for $T_c = 5$ MPa and $T_c = 20$ MPa exhibit some differences. The most salient observation from Fig. 6 is that for $T_c = 20$ MPa during forward transformation, both the localization and propagation occur in a symmetric fashion, specially, with the nucleation of two mirror-image martensite bands at the two grips, followed by the propagation of the multi-finger fronts towards each other, which eventually meet at the mid-point of the tube. On the other hand, no appreciable difference can be observed in regard to the reverse transformation.

It should be emphasized that the subtle details of the transformation pattern (and also of the mechanical response, such as the overshoot stress) are highly susceptible to the experimental setup and its inherent complexities (which are at times intractable) and imperfections, as can be inferred by confronting the experimental results available in the literature and also the insights gained from modeling studies (e.g., Jiang et al., 2017; Rezaee-Hajidehi et al., 2020). This can be also evidenced in the experimental results of Reedlunn et al. (2020a), for instance, in the inconsistent transformation patterns captured under uniaxial tension tests (compare T1 and T3) and combined tension–torsion tests (compare, e.g., P1 and P1b or P5 and P5b), see the corresponding supplemental material (Reedlunn et al., 2020b).

3.4. NiTi tube under simple torsion

This section is aimed at analyzing the simulation results for the case of simple torsion ($\omega = 90°$) and their comparison with the experimental data (case P8) of Reedlunn et al. (2020a). The main emphasis of this analysis is on the formation of longitudinal phase transformation bands and on the key factors that contribute to this phenomenon. These factors include the residual stresses, the collet grips, and the degree of softening/hardening in the intrinsic response under shear. It should be noted that, in the previous section, the limit friction stress of $T_c = 5$ MPa was adopted. This value resulted in a high computational cost as it requires gripped segments of 40 mm length (on each side of the tube) to prevent slippage within the entire grips. Therefore, in this simulation, as well as in the combined tension–torsion simulations presented in Section 3.5, the limit friction stress of $T_c = 20$ MPa is used. This not only reduces the computational cost but also leads to more convincing simulation results, as confirmed by our auxiliary simulations with $T_c = 5$ MPa.

As shown in Fig. 7, the predicted transformation pattern and the mechanical response exhibit some similarities to those observed in the experiment, with the most notable feature being the formation of longitudinal shear bands. In the simulation, the transformation begins with the nucleation of four bands across the entire circumference of the tube, with only one visible in snapshot ‘1’. As the visible band grows to a certain width, a new band nucleates within a hoop distance of approximately 55° (snapshot ‘3’), and another one also at the back side of the tube, thus giving rise to the total of six bands across the entire circumference. Upon further loading, the longitudinal bands start merging (the bands visible in the snapshots merge from the upper grip, while those at the back merge from the lower grip), and proceed like a zipper until the entire free length of the tube is transformed. During unloading, the transformation takes on a different pattern. Rather than the longitudinal bands, the reverse transformation evolves in the form of a helix that shrinks both length-wise and thickness-wise and winds around the tube from the upper grip.

Intriguing differences can be observed between the predicted and experimental transformation patterns. The longitudinal bands in the simulation appear to be slightly more inclined than those in the experiment. In contrast to the experiment, the inclination of the bands is even more pronounced in the reference configuration. While the experimental bands are reported to be non-propagative, some of the fronts in the simulation do propagate, traveling a finite distance of about 15° in the hoop direction. Furthermore, the predicted shear strain variation between the high-strain and low-strain regions reaches up to

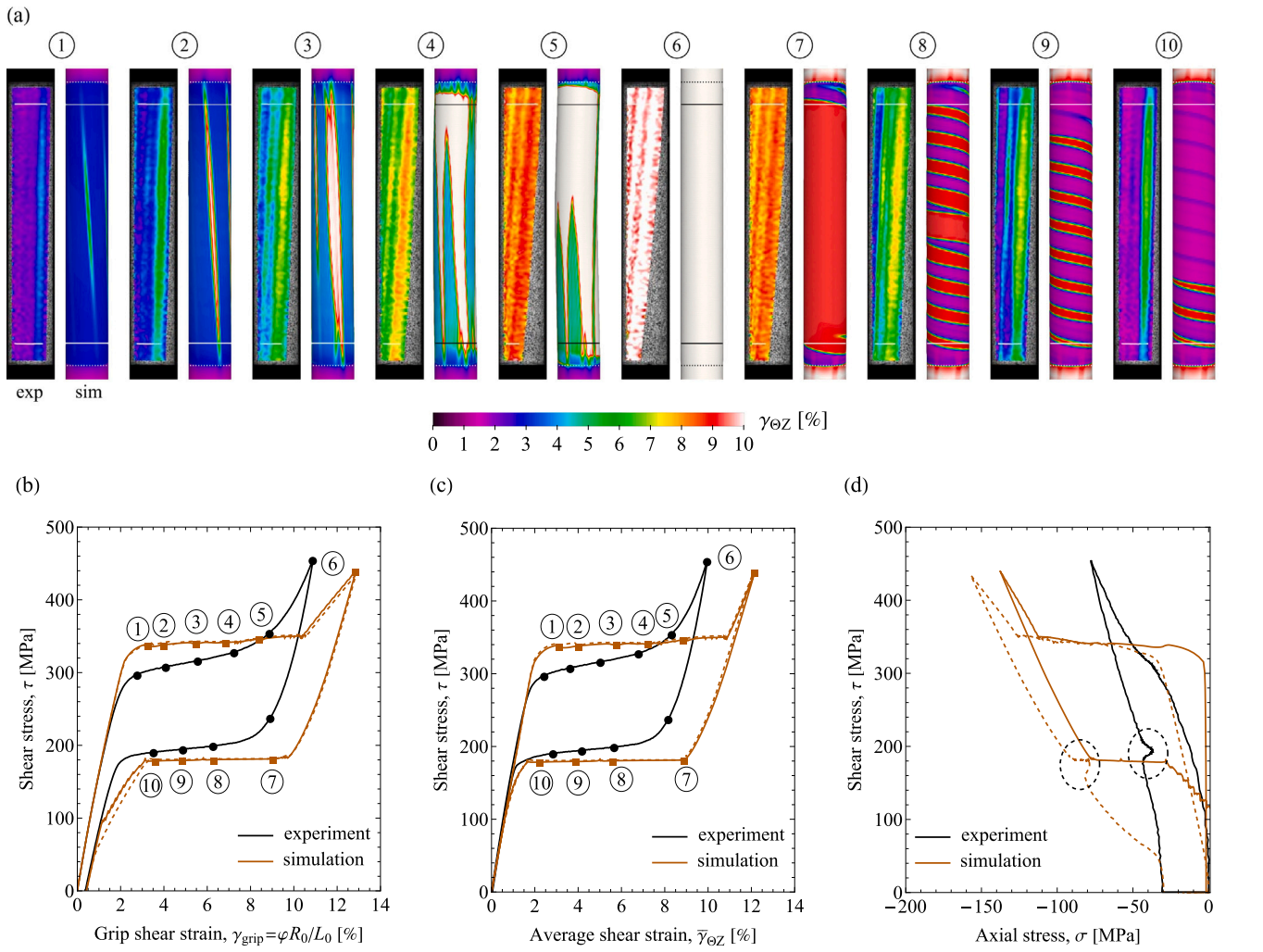

Fig. 7. Simulation results for the case of simple torsion ($\omega = 90°$) and their comparison with the experimental results (case P8) of Reedlunn et al. (2020a): (a) snapshots of the shear strain field $\gamma_{\Theta Z}$, (b,c,d) the global mechanical response represented in terms of (b) shear stress–grip shear strain (τ–γ_{grip}), (c) shear stress–average shear strain (τ–$\bar{\gamma}_{\Theta Z}$), and (d) shear stress–axial stress (τ–σ). The left-hand and right-hand snapshots in panel (a) correspond, respectively, to the experiment (reproduced with permission from Elsevier) and simulation. The dashed curves in panels (b,c,d) represent the response for the case with a radial compression induced by the collet grips.

$\Delta\gamma_{\Theta Z} = 6\%$, which is more than twice the variation measured in the experiment.

Some differences can also be observed in the predicted and experimental mechanical responses. This mainly concerns the transformation-onset stress (overpredicted by the model) and also the hardening behavior. While the experimental shear stress–shear strain curve exhibits significant hardening, a stress plateau is obtained in the simulation, Fig. 7(b,c), which is consistent with the assumed softening intrinsic response, see Fig. 1(c) (the effect of hardening/softening is discussed later in this section). The shear stress–shear strain curves in the simulation exhibit sudden, albeit small, events related to the nucleation and saturation of phase transformation. Notably, the transformation and saturation stages are clearly distinct in the simulation response, while the experimental curve remains smooth throughout. Finally, the shear stress–axial stress (τ–σ) response, Fig. 7(d), reveals an interesting discrepancy between the simulation and the experiment. Specifically, the simulation exhibits a significantly higher compressive axial stress (in fact, a clear stress plateau is visible), which, unlike the experimental results, undergoes a reversal from compressive to tensile stress at the end of the simulation. The underlying causes behind these disparities will be explored in the follow-up study presented below.

We first note that in the experimental setup, since the collets must hold the tube firmly during testing, they exert a certain level of radial compression to the tube's diameter. This compression can lead to a complex stress state at the gripped segments of the tube during the experiment, and hence affecting the global behavior. A new simulation has thus been performed with the grips inducing a radial compression which corresponds to the reduction of the outer radius by about 0.01 mm and results in the axial compressive stress of about 20 MPa. This is then followed by the expansion of the tube in the axial direction to release the resulting axial stresses, and finally by the application of twist. The results of this new simulation are compared to those of the reference simulation in Figs. 7(b,c,d) and 8. The results clearly show negligible changes in the shear stress–shear strain response, however, the shear stress–axial stress (τ–σ) response exhibits some additional similarities to the experimental one. Specifically, the initial elastic slope tends more towards compressive stresses and better agrees with the experimental trend. Although a slightly higher compressive axial stress is developed during loading compared to the simulation with no radial compression at the grips, the reversal of the axial stress (from compressive to tensile) does not occur and the final remnant value is found to be very close to the experimental value. An interesting observation is related to the initiation of reverse transformation during unloading, where a relatively sharp axial stress bump, as marked by the dashed circle in Fig. 7(d), can be seen, which closely resembles the analogous experimental event and is indicative of a modified stress state caused by the compression induced by the collet.

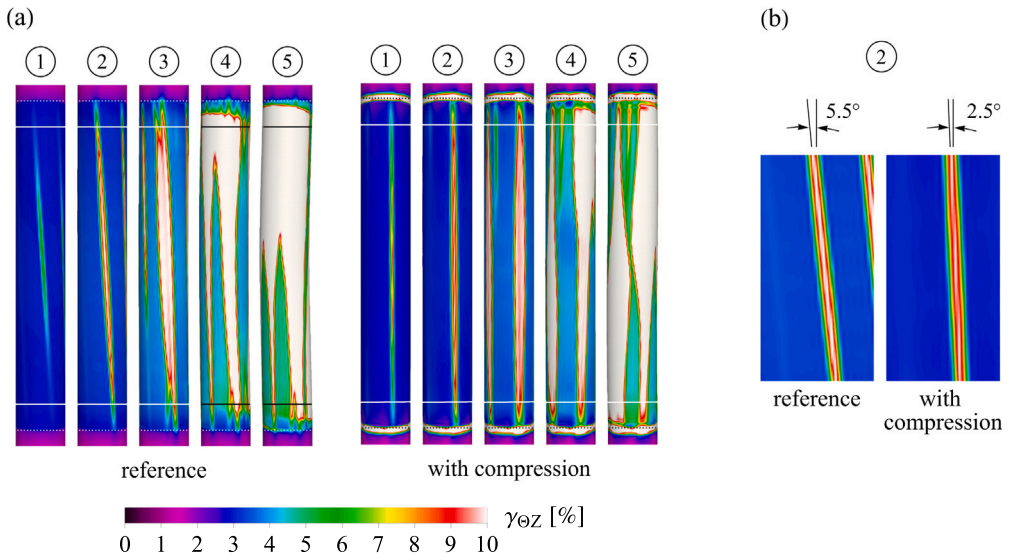

Fig. 8. The impact of the radial compression induced by the collet grips on the transformation pattern during loading (a) and the orientation of the longitudinal bands (b) in simple torsion. The close-up views in panel (b) are taken in the undeformed and unwrapped-tube configuration.

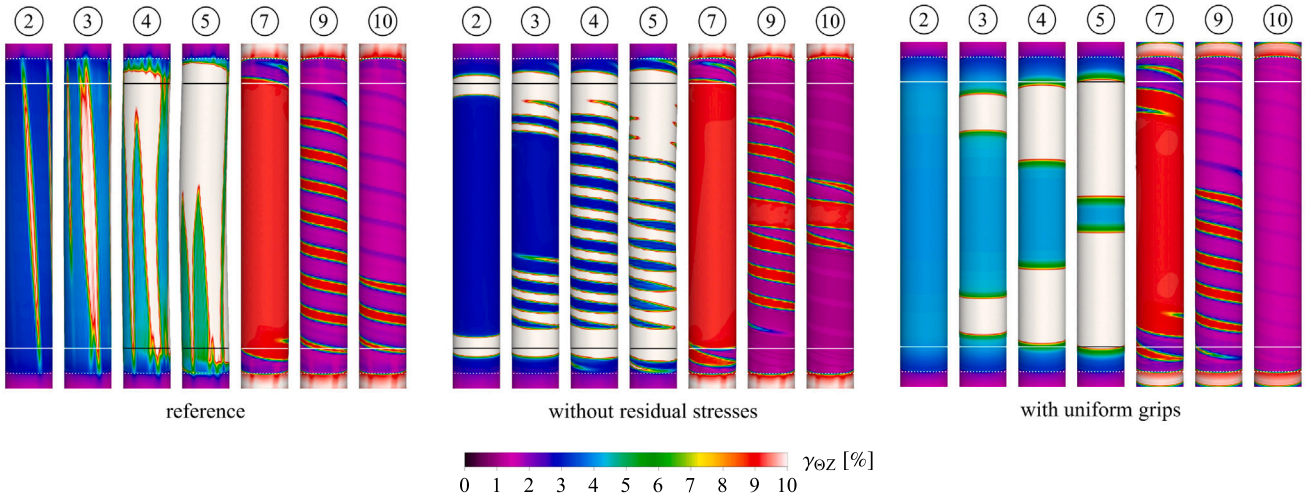

Fig. 9. The impact of residual stresses and collet grips on the transformation pattern in simple torsion. In the reference simulation, both the residual stresses and the non-uniformity of the collet grips are accounted for.

The examination of the transformation pattern also reveals some noticeable differences. As shown in Fig. 8, the longitudinal bands in the new simulation are less inclined, with the inclination angle (measured in the reference and unwrapped-tube configuration) that is more than twice lower than that in the reference simulation, and thus is a closer match to the nearly straight orientation observed in the experiment. Additionally, evident variations in the way the longitudinal bands merge can also be observed, see snapshots '4' and '5'.

We now perform a detailed investigation on the formation of peculiar longitudinal shear bands, with the aim to unravel the underlying factors promoting them. According to Reedlunn et al. (2020a), the residual stresses associated with prior incompatible plastic deformation can be a potential driving force for the formation of longitudinal bands. The authors also assert that the formation of these bands is not an outcome of the non-uniformity dictated by the collets (as confirmed by the experiment where copper sleeves were inserted within the grips with the aim to mitigate the non-uniformity). With these considerations in mind, we seek to delineate the impact of these elements on the formation of longitudinal bands. Additional simulations have thus been carried out, one with no residual stresses (i.e., for $\epsilon_R = 0$ and $\epsilon_Z = 0$, see Appendix A.1), and another one with uniform grips (i.e., with uniform tube–grip contact surfaces).

Secondly, we note that the non-hardening intrinsic response in shear is presumed to be a crucial prerequisite for the localization of phase transformation bands under torsion (as in the reference case reported in Fig. 7). Therefore, it is also of particular interest to examine the sensitivity of the transformation pattern and global mechanical response to the intrinsic response in shear. To this end, the simple torsion simulation has been repeated for a range of intrinsic responses, i.e., from an isotropic material with a strong softening behavior (the case with $\beta = 1.4$) to a highly transversely isotropic material with a strong hardening behavior (the case with $\beta = 1$), as illustrated in Fig. 10(b). Recall that parameter β determines the degree of transverse isotropy, see the related discussion in Section 2. An alternative study could be conducted by altering the softening modulus H_T. However, in this scenario, not only the softening/hardening behavior in shear would be affected, but also that in tension. At the same time, the anisotropy would remain the same.

Fig. 9 illustrates the impact of the residual stresses and (non-uniform) collet grips on the transformation pattern. It is interesting

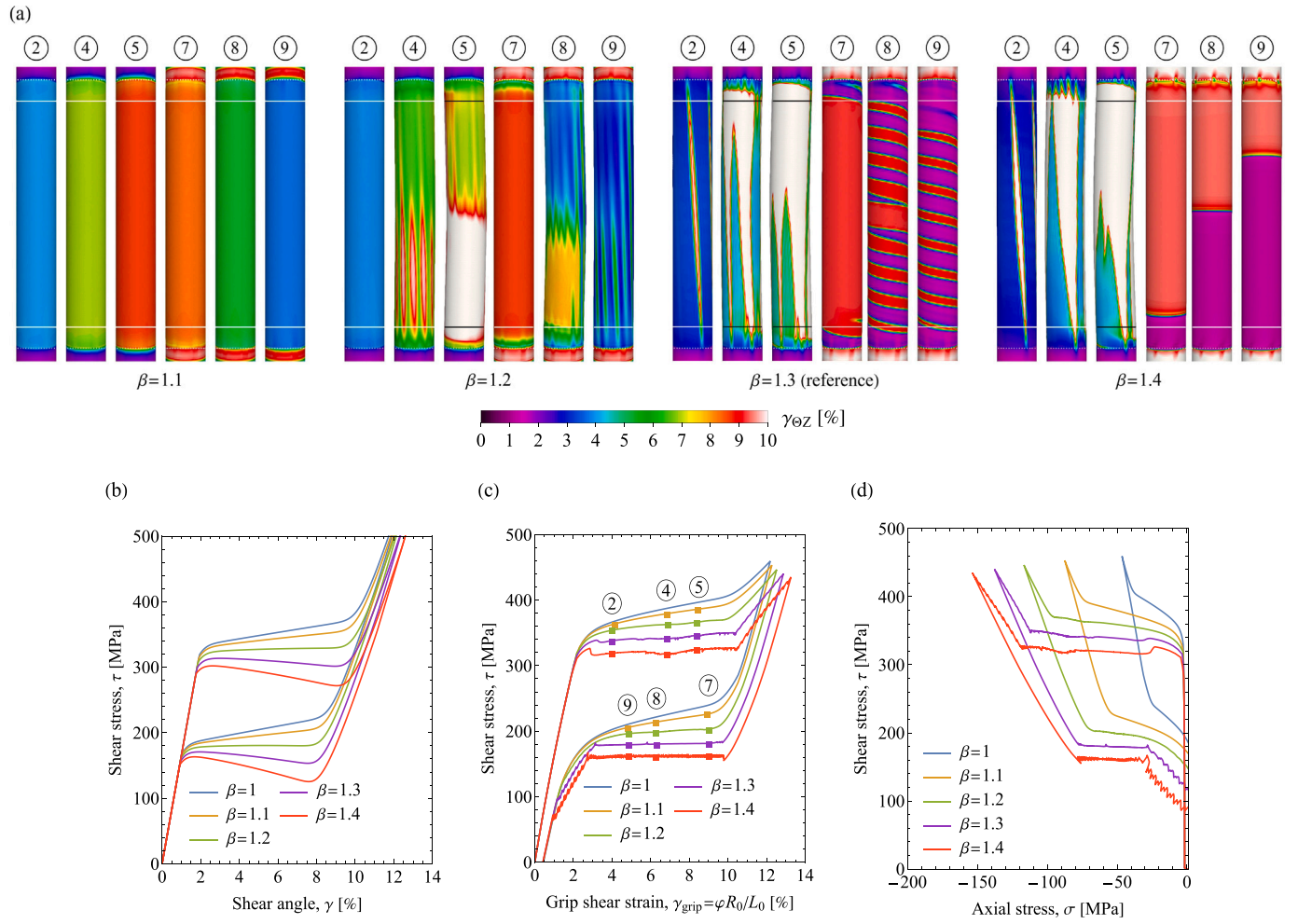

Fig. 10. The effect of parameter β, controlling the degree of transverse isotropy, on the transformation pattern and on the mechanical response in simple torsion: (a) snapshots of the shear strain field $\gamma_{\Theta Z}$, (b) the intrinsic response in shear, (c) the global shear stress–grip shear strain (τ–γ_{grip}) response, and (d) the global shear stress–axial stress (τ–σ) response. The case with $\beta = 1.3$ represents the reference simulation. Note that the homogeneous transformation obtained for $\beta = 1$ is roughly the same as that of $\beta = 1.1$, and thus is not shown in panel (a).

to notice that the transformation pattern varies in each scenario and only when both factors are accounted for do the longitudinal bands form. In the absence of residual stresses, the transformation initiates as two separate helices at both grips, which then proceed to merge in the middle of the tube. On the other hand, when using uniform grips, the transformation initiates in the form of sharp ring fronts at both grips and maintains this pattern throughout the process. In fact, the two reported patterns are the natural patterns that one would expect to occur, if at all, under torsion. During unloading, the transformation pattern consistently appears as a helix. It is worth noting that we also examined cases with both factors present, however, with a somewhat lower intensity of residual stresses. In particular, we set either of the two strain components ϵ_{R} and ϵ_{Z} equal to zero and calibrated the other one such that the desired curvature is obtained, see the related discussion in Appendix A.1. It was found that the corresponding residual stresses were not sufficient to induce the formation of longitudinal bands. In summary, it is the synergistic impact of the two factors, with an adequate intensity of residual stresses, that ultimately gives rise to longitudinal bands.

Our results on the relationship between the intrinsic response and global behavior (Fig. 10) indicate that the longitudinal bands develop even when the intrinsic response is not characterized by softening, as in the case of $\beta = 1.2$ with a minimal level of hardening. The bands, however, do not span the entire length of the tube. The noticeable features of the global response for $\beta = 1.2$ involve a smooth shear stress–grip shear strain (τ–γ_{grip}) curve, the formation of the total of 10 longitudinal bands, a strain variation of about $\Delta\gamma_{\Theta Z} = 3\%$ between the high-strain and low-strain regions, non-propagative fronts, and most importantly, appearance of longitudinal bands during the reverse transformation (actually, the reverse transformation evolution seems to closely mirror the pattern of the forward transformation). Conversely, in the case with the strongest softening ($\beta = 1.4$), a single ring front appears during unloading, while the other features are similar to that of our reference simulation ($\beta = 1.3$). The dissimilar reverse transformation patterning can be attributed to the fact that stronger softening leads to higher energy of diffuse interfaces (macroscopic transformation fronts), and thus the propensity towards patterns with lower interfacial area (Feng and Sun, 2006), as in the case of $\beta = 1.4$ with a sharp ring front. Finally, Fig. 10(d) shows that as β approaches unity (i.e., as the degree of transverse isotropy increases), the compressive axial stress produced during torsion decreases, and at the same time, a transition from a plateau-type response to a hardening-type response is observed.

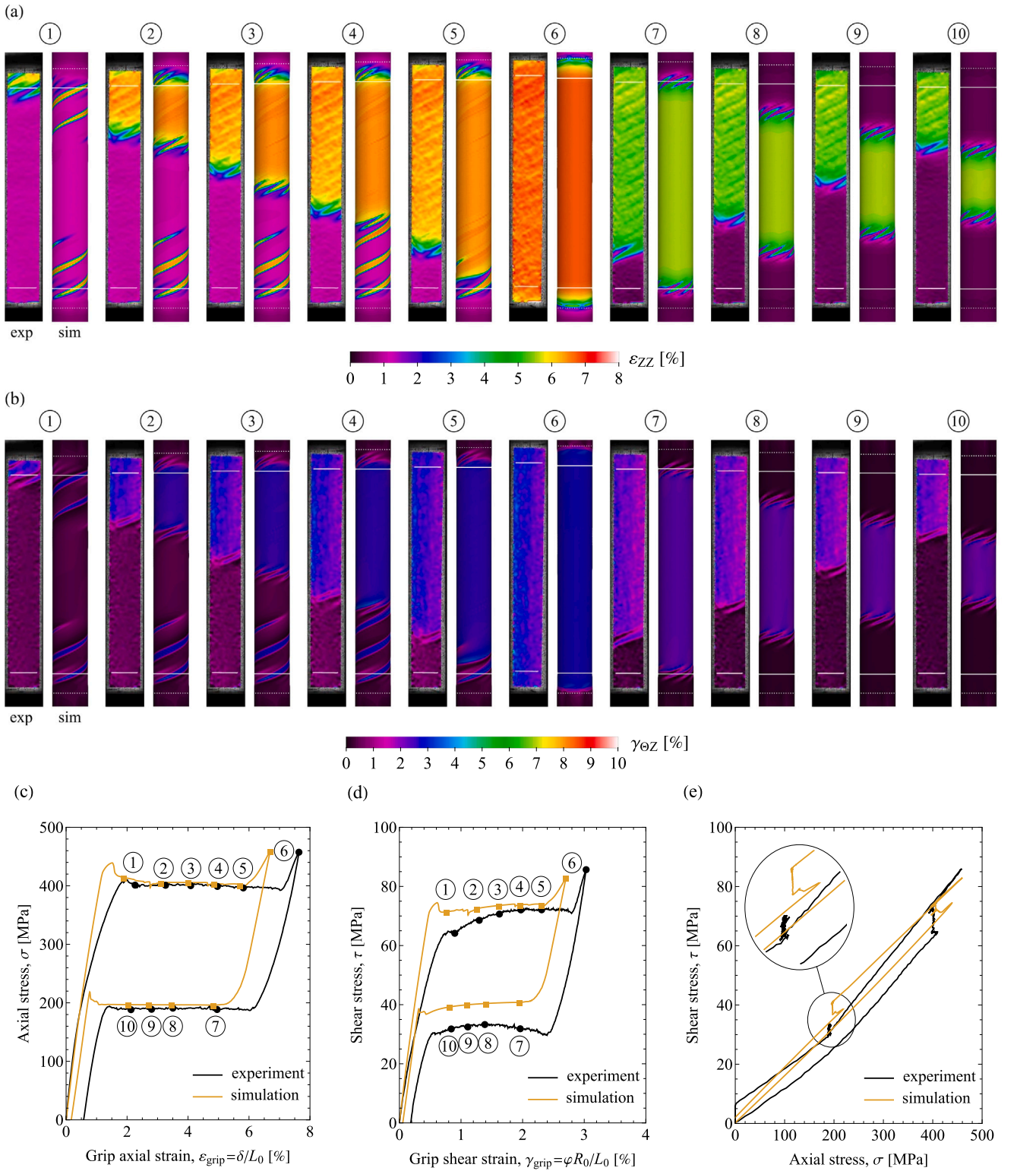

Fig. 11. Simulation results for the case of combined tension–torsion at $\omega = 22°$ and their comparison with the experimental results (case P1) of Reedlunn et al. (2020a). The left-hand and right-hand snapshots in panels (a) and (b) correspond, respectively, to the experiment (reproduced with permission from Elsevier) and simulation.

3.5. NiTi tube under combined tension–torsion

The transformation pattern and the mechanical response for combined tension–torsion loading, corresponding to strain-path angles of $22° \leq \omega \leq 84°$, are presented in Figs. 11–17. The simulation results, together with their comparison with the experimental ones, reveal several interesting features. Although some discrepancies, which are at times substantial, can be noticed, overall, the simulation results exhibit a high level of consistency with the experimental ones. In the following, we summarize the most important observations. Note that from now

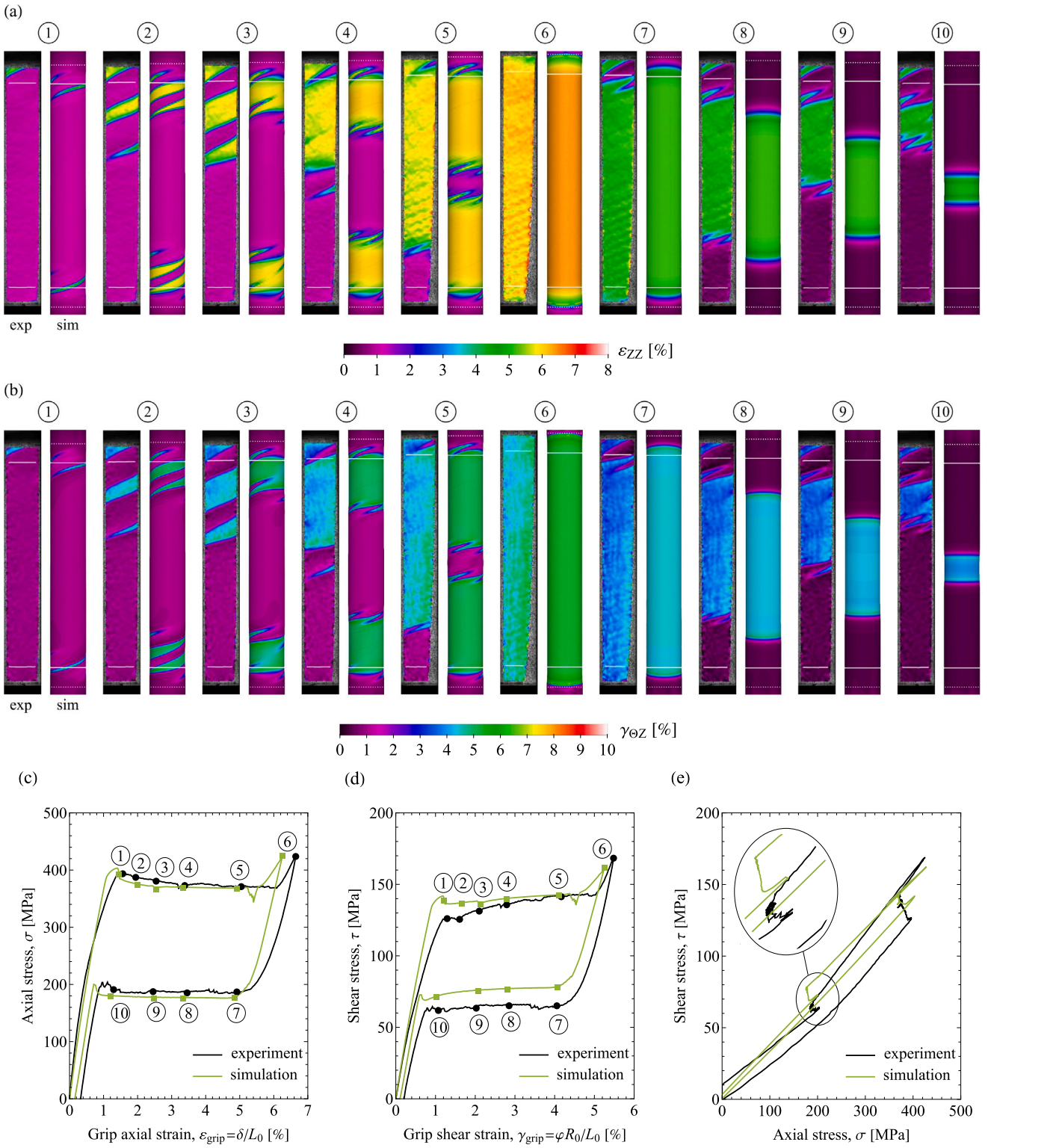

Fig. 12. Simulation results for the case of combined tension–torsion at $\omega = 40°$ and their comparison with the experimental results (case P2) of Reedlunn et al. (2020a). The left-hand and right-hand snapshots in panels (a) and (b) correspond, respectively, to the experiment (reproduced with permission from Elsevier) and simulation.

on our focus is primarily on the mechanical responses in terms of the grip strains ε_{grip} and γ_{grip}. This preference stems from the fact that grip slippage plays an important role in our analysis, and it is therefore pertinent to present the 'unfiltered' mechanical responses σ–ε_{grip} and τ–γ_{grip} that reflect the impact of grip slippage. For completeness, a selection of σ–$\bar{\varepsilon}_{ZZ}$ and τ–$\bar{\gamma}_{\Theta Z}$ responses are provided in Appendix F.

The transformation patterns for $22° \leq \omega \leq 63°$ demonstrate a consistent trend. The transformation always initiates with the nucleation of two separate helical bands at each grip, followed by the growth of the helices in the transverse direction, and the subsequent emergence of a multi-finger front and its progression (either from one grip as for $\omega = 22°$ or from both grips as for $\omega = 40°$, 53°

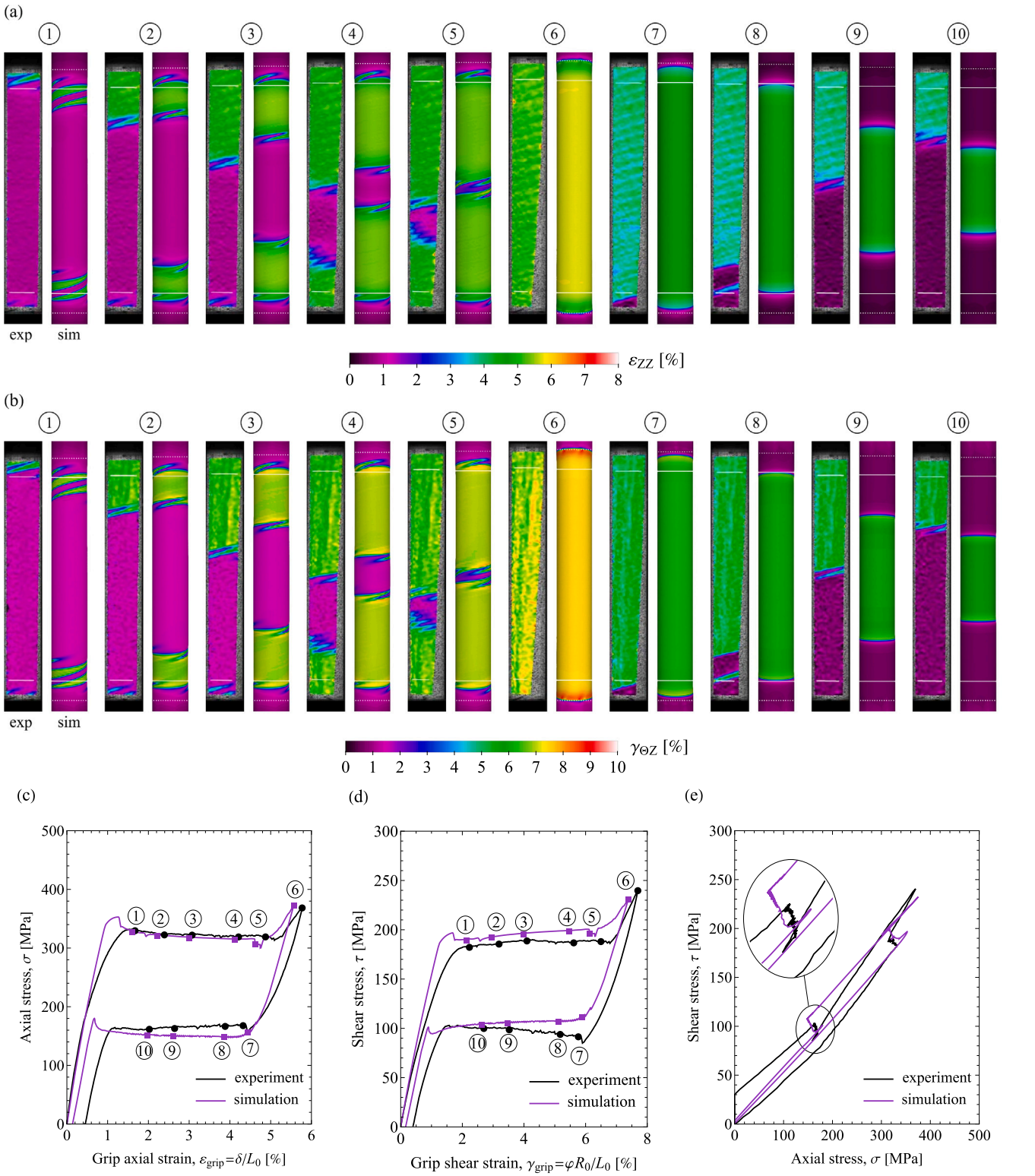

Fig. 13. Simulation results for the case of combined tension–torsion at $\omega = 53°$ and their comparison with the experimental results (case P3) of Reedlunn et al. (2020a). The left-hand and right-hand snapshots in panels (a) and (b) correspond, respectively, to the experiment (reproduced with permission from Elsevier) and simulation.

and 63°) until the complete transformation of the tube. The orientation of the incipient helical bands and fingers, the axial length of the bands, and the number of fingers are observed to vary with the strain-path angle ω. In particular, as ω increases, the bands tend to align perpendicularly to the tube axis, become shallower, and the number of fingers diminishes (ranging from 6 fingers over the entire circumference of the tube for $\omega = 22°$ to one finger for $\omega = 63°$). A similar observation was made in our previous study pertaining to non-proportional torsion-then-tension loading conditions (Rezaee-Hajidehi and Stupkiewicz, 2021).

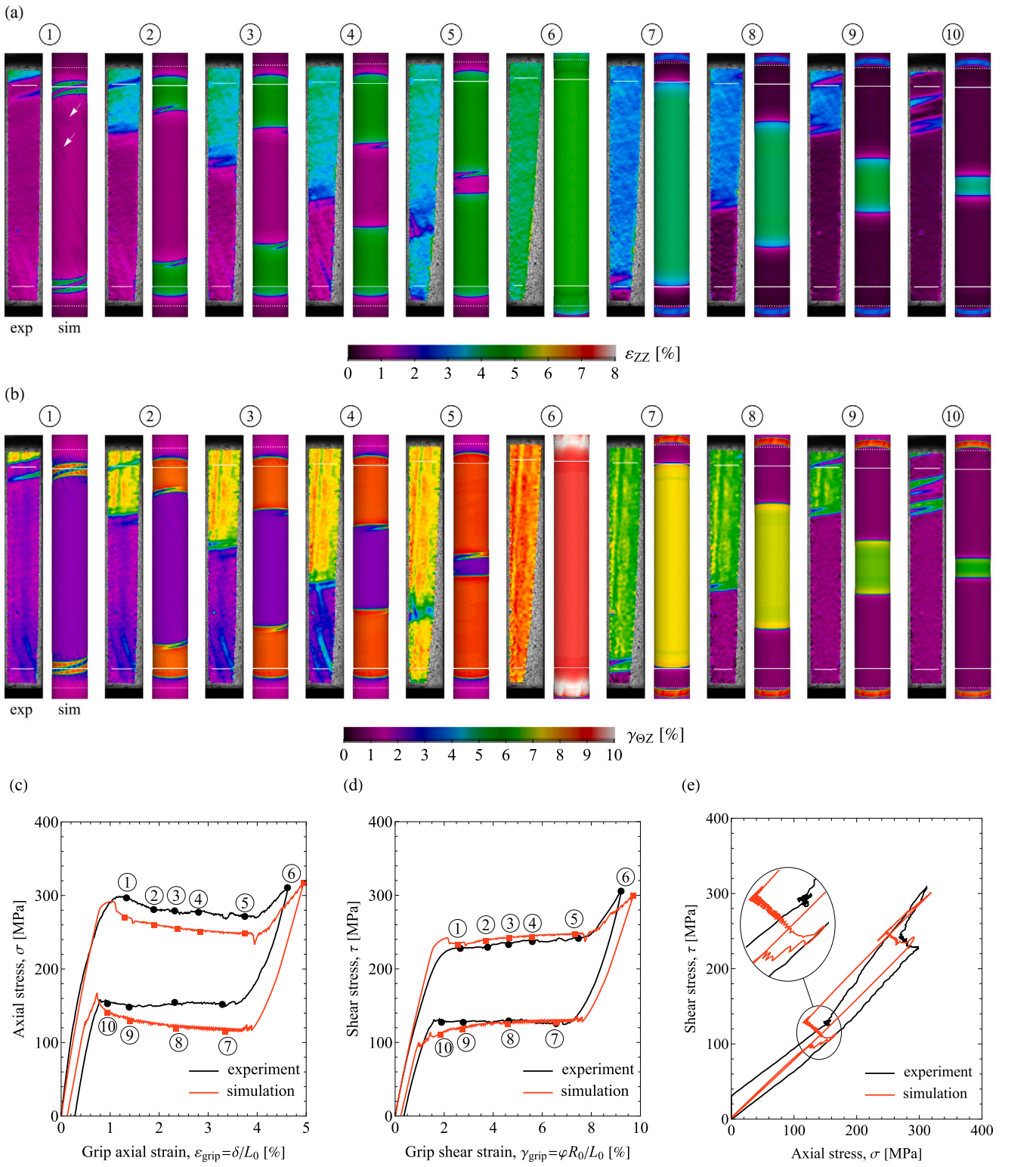

Fig. 14. Simulation results for the case of combined tension–torsion at $\omega = 63°$ and their comparison with the experimental results (case P4) of Reedlunn et al. (2020a). The left-hand and right-hand snapshots in panels (a) and (b) correspond, respectively, to the experiment (reproduced with permission from Elsevier) and simulation.

The transformation pattern for $\omega = 71°$ deviates from that manifested for $22° \le \omega \le 63°$. In this case, the two incipient bands extend axially across the entire free length of the tube, and subsequently branch at the tail as they grow in the transverse direction, as depicted in snapshot '2' in Fig. 15. Another distinguishing feature is the occurrence of a secondary transformation front that emanates from the bottom grip and takes the form of nearly horizontal fingers, see snapshots '3' and '4'. These fingers grow and coalesce into the primary bands in a successive order, and ultimately merge them, akin to the action of a zipper. Henceforth, the transformation progresses via a diffuse ring front, see snapshot '6'.

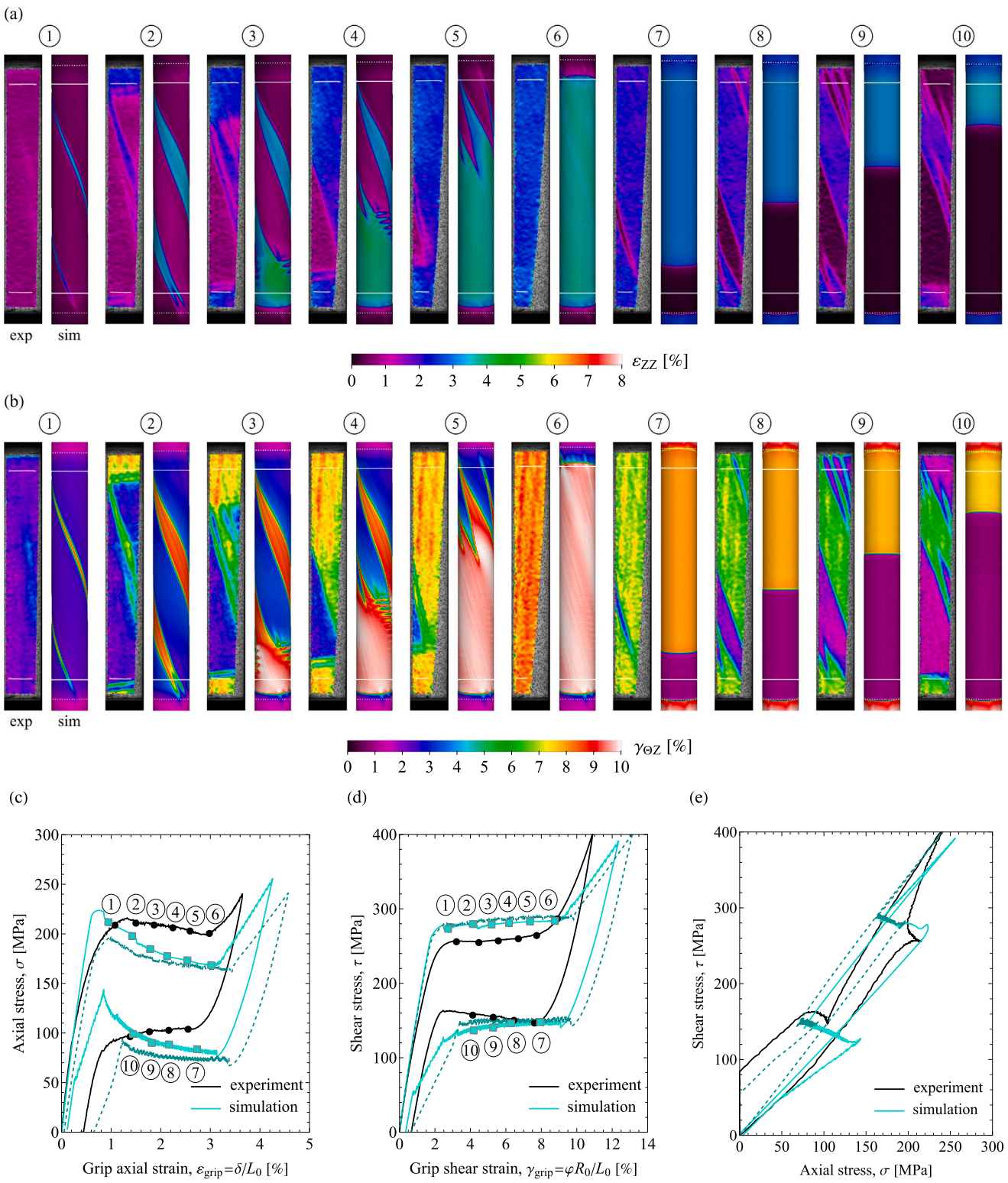

Fig. 15. Simulation results for the case of combined tension–torsion at $\omega = 71°$ and their comparison with the experimental results (case P5) of Reedlunn et al. (2020a). The left-hand and right-hand snapshots in panels (a) and (b) correspond, respectively, to the experiment (reproduced with permission from Elsevier) and simulation. The dashed curves represent the mechanical response for the case with a radial compression induced by the collet grips.

The torsion-dominated strain paths $\omega = 78°$ and $\omega = 84°$ exhibit a transformation pattern similar to $\omega = 71°$. In both cases, longitudinal bands form along the free length of the tube, where the orientation of the bands becomes less inclined with respect to the tube axis as ω increases. Unlike in $\omega = 71°$, no secondary front develops and the bands merge from both the top and bottom grips. It can be observed that the pattern for $\omega = 78°$ and $\omega = 84°$ is quite similar to that under simple torsion (Fig. 7).

A majority of the observations detailed above for $22° \leq \omega \leq 84°$ agree nicely with the experiment (cases P1–P7). Clearly, there are some differences, as discussed below.

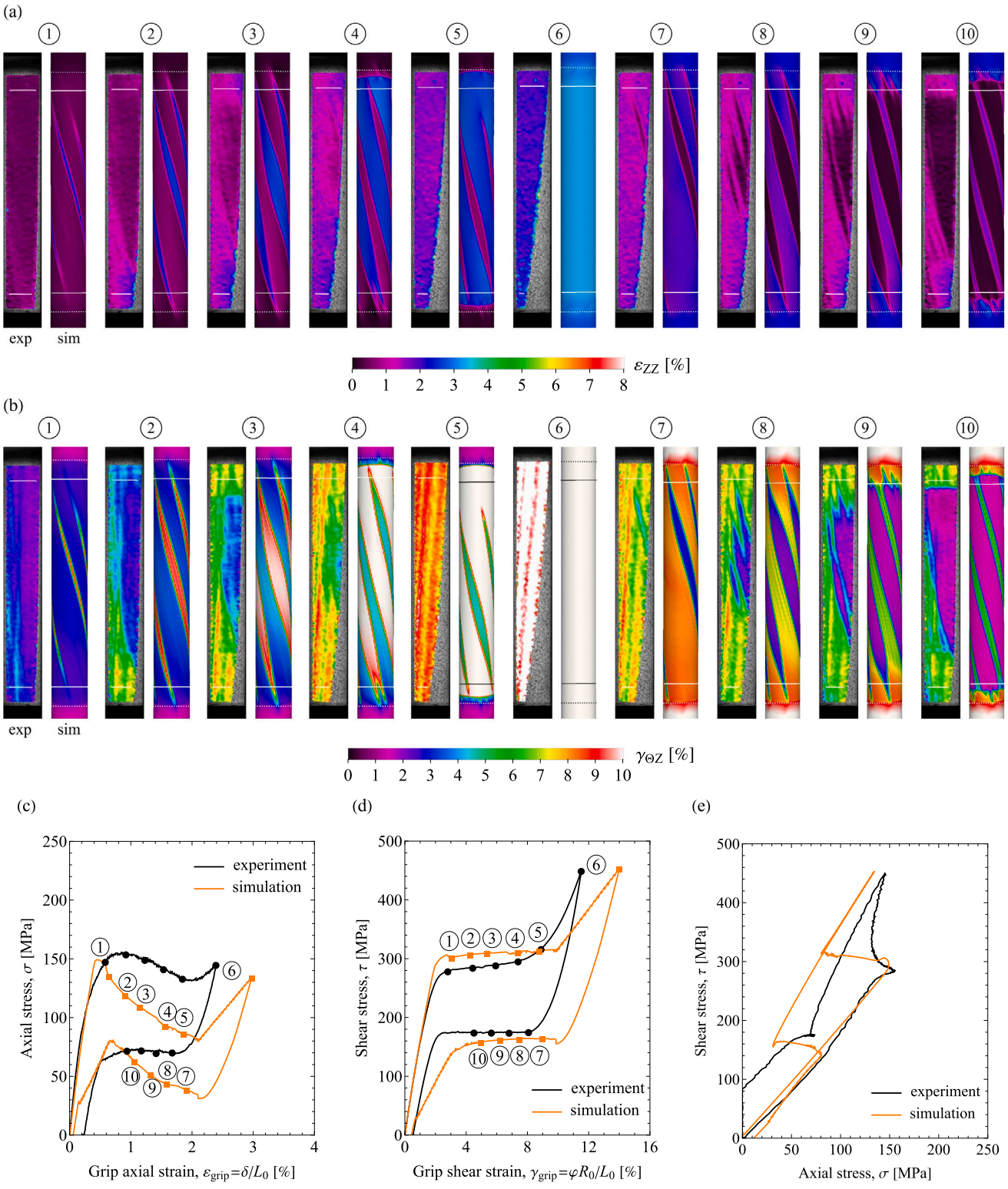

Fig. 16. Simulation results for the case of combined tension–torsion at $\omega = 78°$ and their comparison with the experimental results (case P6) of Reedlunn et al. (2020a). The left-hand and right-hand snapshots in panels (a) and (b) correspond, respectively, to the experiment (reproduced with permission from Elsevier) and simulation.

One of the eye-catching differences between the simulation and experimental results pertains to the pattern of reverse transformation. With the exception of the lowest strain-path angle $\omega = 22°$ and the torsion-dominated case $\omega = 78°$, the reverse transformation consistently exhibits relatively sharp ring fronts (i.e., with no fingers) that shrink either concurrently from the both grips or only from the bottom grip. Recall that a quite similar pattern was observed in the case of simple torsion ($\omega = 90°$) with a transverse isotropy parameter of $\beta = 1.4$, i.e., with a strong softening in the intrinsic response, see Fig. 10. While there may be some apparent resemblance between this pattern and

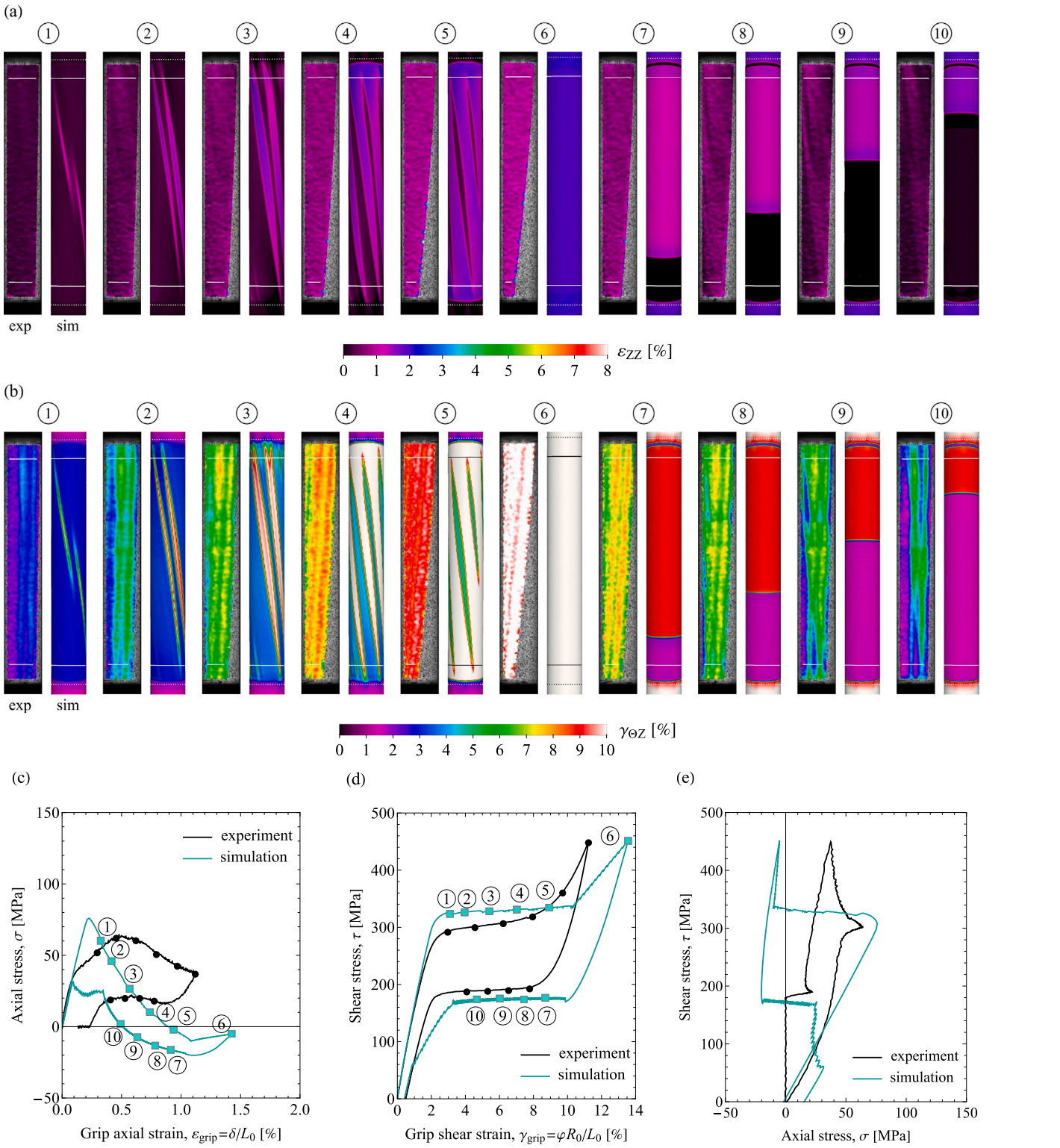

Fig. 17. Simulation results for the case of combined tension–torsion at $\omega = 84°$ and their comparison with the experimental results (case P7) of Reedlunn et al. (2020a). The left-hand and right-hand snapshots in panels (a) and (b) correspond, respectively, to the experiment (reproduced with permission from Elsevier) and simulation.

those from the experiment for $\omega = 53°$ (case P3) and $\omega = 63°$ (case P4), we contend that this resemblance is not indicative of a genuine correlation, as in the simulation the ring pattern is observed for the majority of the strain-path angles ω. It is possible that the lack of an authentic agreement between the predicted and experimental reverse transformation patterns is associated with the crucial role played by the interfacial energy and its preference for minimal interfacial area, as discussed at the end of Section 3.4. Nevertheless, it remains unclear why this preference is not evidenced for all strain-path angles ω. Another factor that may explain the observed disagreement is the initial conditions for transformation. While the initial conditions for the forward transformation closely match those in the experiment (both starting

from an untransformed state), the corresponding initial conditions for the reverse transformation deviate to some extent. This is partly due to the simplified grip description in the simulations, which results in a different distribution of slippage within the collets compared to the experiment, and partly due to the inability of the model to fully capture the striations, see the discussion provided later.

Furthermore, for torsion-dominated strain paths ($63° \le \omega \le 90°$), the unloading snapshots reveal the presence of isolated domains of martensite within the gripped segments of the tube. As the experimental snapshots do not provide visual evidence of the transformation pattern in the gripped segments, the validity of this observation remains inconclusive.

A number of additional features are also discernible in the predicted transformation patterns, reminiscent of those observed in the experiment. Of particular interest is the appearance of faint striations. The striations, which were not evident under uniaxial tension ($\omega = 0°$) and simple torsion ($\omega = 90°$), are the vestiges of incipient bands, and are clearly apparent in cases with adequately long bands, as can be seen, for instance, in snapshot '5' in Fig. 11 and in snapshot '6' in Fig. 15. As previously noted in Section 3.3, an enhanced model that accounts for a more accurate description of martensite reorientation would probably be required to fully capture the striations. Another noteworthy feature is the emergence of islands of slightly elevated strains in the case with $\omega = 63°$ (see the arrows in snapshot '1' in Fig. 14), indicating potential sites for the nucleation of a secondary front. Unlike the analogous experiment, where these islands evolve into a secondary front (see experimental snapshots '1'–'4' in Fig. 14), in this simulation, the islands possess a transient nature and disappear shortly after they emerge. Finally, a strong similarity can be observed between the reverse transformation patterns obtained for $\omega = 22°$ and $\omega = 78°$ and those from the experiment. Especially, $\omega = 78°$ displays a number of subtle features that closely match those in the experiment, see e.g., snapshots '8' and '9' in Fig. 16.

The analysis of the transformation patterns is now complemented by a detailed examination of the mechanical responses. From Figs. 11–17(c,d) it is immediate to see that as the value of ω is increased, the axial stress decreases while the shear stress increases. The predicted responses demonstrate sharp stress drops concomitant with the nucleation of incipient helical bands, visible in both axial and shear responses. It can be seen that as ω alters from tension-dominated to torsion-dominated strain paths, the axial stress within the transformation branch shows a declining trend, manifesting as a transition from a plateau-like response to a softening-like response, as is evident for $63° \le \omega \le 84°$. Such a declining trend is also present in the experimental responses, though with a less pronounced rate of plateau-to-softening transition. In contrast to the axial response, the shear response, regardless of the value of ω, exhibits a distinct stress plateau with a mild degree of apparent hardening. During unloading, qualitatively similar behavior is observed. While the initiation of reverse transformation does not always provoke sharp stress events, the reverse transformation saturation is often accompanied by distinct stress rises, particularly noticeable in the axial response for the torsion-dominated cases, $63° \le \omega \le 84°$. It is worth noting that the axial and shear responses for $\omega = 63°$ and $\omega = 71°$ display visible stress oscillations during unloading, which are traced to the pinning of the (relatively sharp) interfaces to the finite-element nodes as the ring front traverses the tube.

A comparison of the shear stress–axial stress (τ–σ) responses obtained from the simulation and from the experiment, see Figs. 11–17(e), discloses some characteristic differences, in particular, in relation to the stress trajectory during unloading and the remnant stress at the end of the loading–unloading cycle. A closer examination indicates that these differences can be partially attributed to the use of an isotropic friction model that does not account for the slippage anisotropy in the axial–circumferential plane. Furthermore, the lack of the radial compression imparted by the collet is also a contributing factor. The latter is further supported by an additional simulation performed for the case of $\omega = 71°$ incorporating this radial compression, see the dashed curves in Fig. 15(c–e). As in the case of simple torsion, this radial compression amounts to the reduction of the outer radius by about 0.01 mm.

A summary of the predicted mechanical responses is presented in Fig. 18, where panels (a,b,c) depict the loading responses and panels (d,e,f) depict the unloading responses. The progression of the mechanical responses as a function of the strain-path angle ω is clearly visible in the plots. Additionally, to illustrate the final remnant stresses, the plots have been extended to negative stress values. Superimposed on the τ–σ plots are the characteristic stress points, with cross symbols denoting the experimentally-determined forward/reverse transformation-onset stresses and blue circles denoting those extracted from the simulation results. It is important to note that the approach by which the characteristic stress points are determined is a subject of dispute, as discussed in great detail in our previous study (Rezaee-Hajidehi and Stupkiewicz, 2021). In an effort to maintain consistency with the experiment, we have chosen to adopt a similar approach (with certain simplifications) as that employed by Reedlunn et al. (2020a), see Appendix A therein. The approach hinges on the mechanical response in terms of the normalized equivalent measures $\bar{\sigma}_{\mathrm{eq}} = \sigma_{\mathrm{eq}}/\sigma_{\mathrm{T}}^{*}$ and $\bar{\varepsilon}_{\mathrm{eq}} = \varepsilon_{\mathrm{eq}}/\varepsilon_{\mathrm{T}}^{*}$, where $\sigma_{\mathrm{eq}} = \sqrt{\sigma^2 + 3\tau^2}$ and $\varepsilon_{\mathrm{eq}} = \sqrt{\bar{\varepsilon}_{ZZ}^2 + \bar{\gamma}_{\Theta Z}^2/3}$ are computed by using the von Mises criteria and the normalization is done with respect to the plateau stress σ_{T}^{*} and the (stress-free) transformation strain $\varepsilon_{\mathrm{T}}^{*}$ (see the discussion below) associated with uniaxial tension. The forward/reverse transformation-onset stress is then identified as the first point on the loading/unloading curve with a tangent slope $\mathrm{d}\bar{\sigma}_{\mathrm{eq}}/\mathrm{d}\bar{\varepsilon}_{\mathrm{eq}}$ equal to unity. Unlike Reedlunn et al. (2020a), we have employed the same approach for all tension–torsion and compression–torsion strain paths, see Fig. 25 and the related discussion in Section 3.6. Overall, a satisfactory agreement is found between the experimental and simulation loci for the tension-dominated paths, while a notable divergence is detected for the torsion-dominated paths, which is further elaborated in the following discussion.

To get a holistic overview, the predicted transformation-onset stress and transformation strain loci for the entire tension–torsion–compression range (the compression–torsion strain paths are discussed in Section 3.6) are compared in Fig. 19 with those measured by Reedlunn et al. (2020a). The axial and shear transformation strains (denoted by ε^{*} and γ^{*}) represent the stress-free strains and are determined, in a way consistent with Reedlunn et al. (2020a), at the intersection between the extended elastic unloading branch of the axial and shear responses with the respective zero-stress axes. Superimposed on the plots are also the transformation loci corresponding to the intrinsic responses resulting from the model and the parametric ellipse proposed by Reedlunn et al. (2020a). It can be observed that the predicted and experimentally-measured loci are in an overall good agreement with each other. A noticeable overprediction of the transformation-onset stresses is discernible for the torsion-dominated paths, which is somewhat mitigated when the intrinsic locus is used as a reference for comparison. It should be remarked that the main reason for the discrepancy between the simulated-tube and intrinsic responses of the model is that the shear stress in the finite-element simulations is computed at the outer surface of the tube (recall that $\tau = M D_0/(2J_0)$). This also explains the aforementioned overprediction, as the material parameters are calibrated to obtain the desired agreement between the *intrinsic* responses of the model and the tube responses from the experiment. At the same time, the finite thickness of the tube (which leads to an inhomogeneous shear stress across the thickness) and the residual stresses within the tube may also contribute to this discrepancy. Furthermore, our characterization of the (forward and reverse) transformation-onset stresses has some simplifications with respect to that used by Reedlunn et al. (2020a), which may also be a contributing factor to the observed discrepancy.

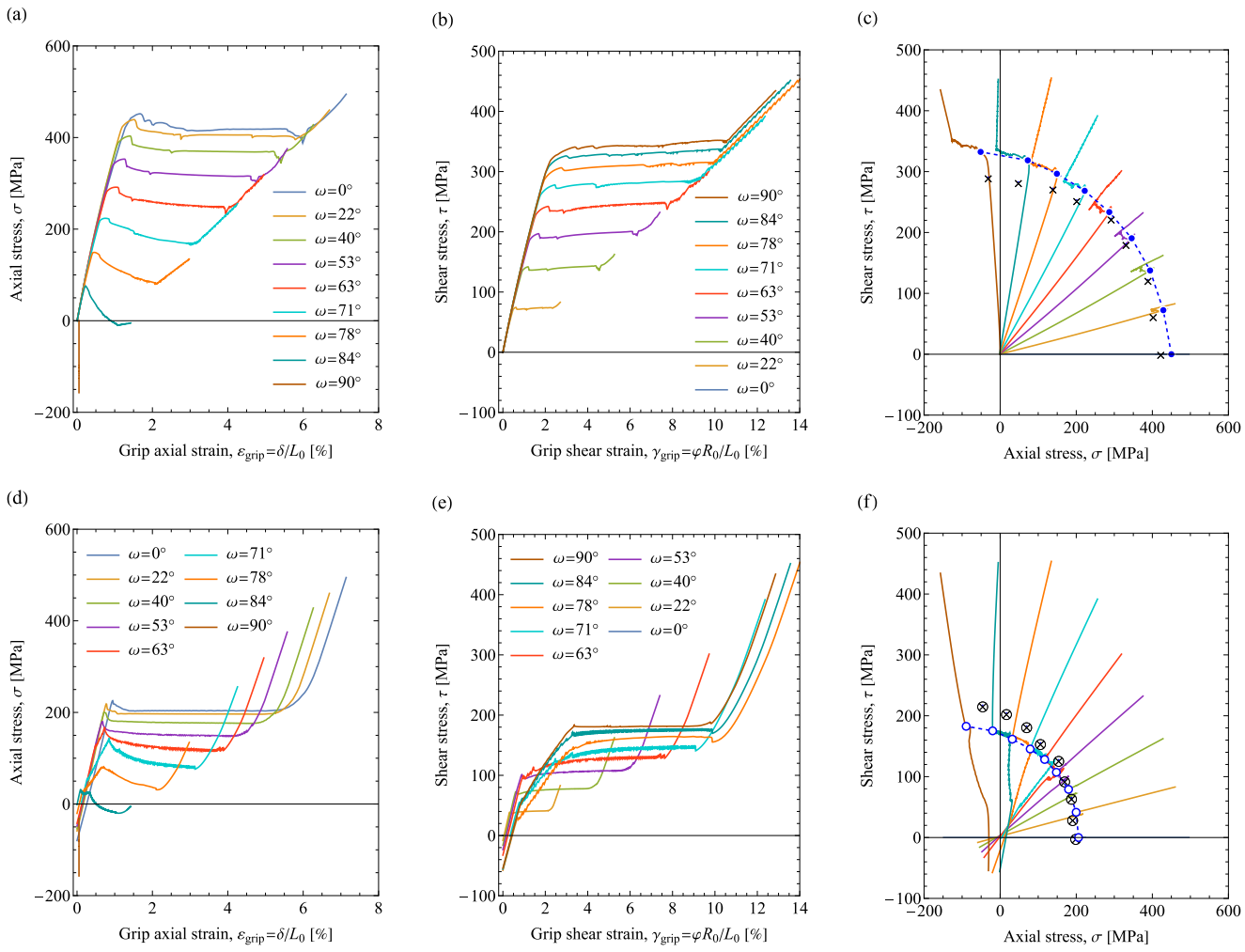

Fig. 18. Global mechanical responses in combined tension–torsion: (a,b,c) loading stage, and (d,e,f) unloading stage. The blue circles in panels (c,f) denote the characteristic transformation stresses extracted from the simulation results, while the cross markers denote the analogous experimental points. All cases, including uniaxial tension (see Fig. 4), correspond to the limit friction stress of $T_c = 20$ MPa. The response for simple torsion ($\omega = 90°$) corresponds to the case with an initial radial compression induced by the collets.

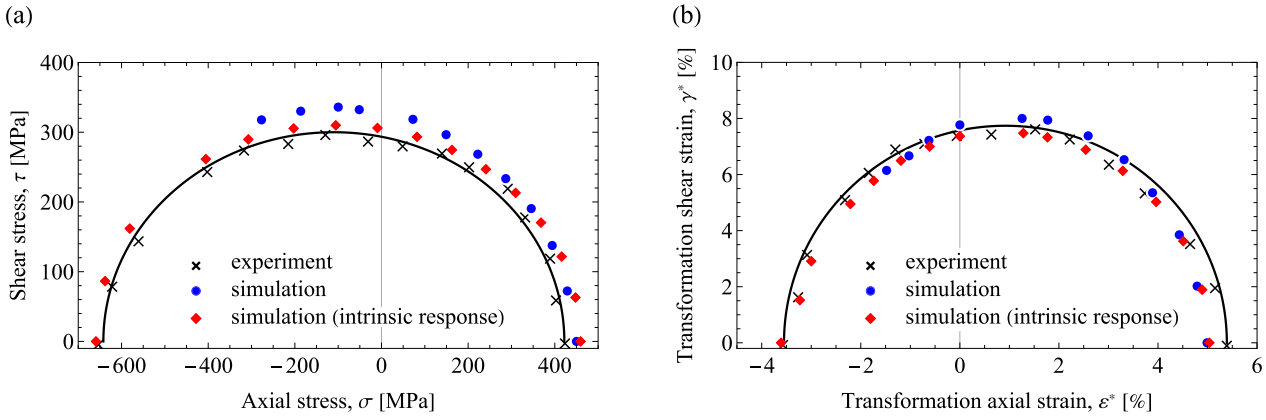

Fig. 19. The predicted transformation-onset stress and transformation strain loci and their comparison with the experimental results of Reedlunn et al. (2020a). The superimposed ellipses (solid lines) are the parametric surfaces proposed by Reedlunn et al. (2020a) and are fitted to the experimental data, see their Fig. 26.

We wrap up this section with a brief analysis of the transformation front orientation. Close-up views of the front (taken in the reference and unwrapped-tube configuration) within the full tension–torsion quadrant ($0° \le \omega \le 90°$) are provided in Fig. 20, highlighting that the simulations have successfully captured the various subtle features of the transformation patterns, such as the tendency of the front towards a perpendicular alignment to the tube axis as ω enters torsion-dominated region, the transition to longitudinal bands that occurs at $\omega = 71°$, and the nearly straight orientation of the bands under simple torsion. To quantitatively validate the findings, we have compared our measurements of the front trailing-edge and leading-edge angles (α_1 and α_2, respectively) to the experimental data, as shown in Fig. 21. Note that,

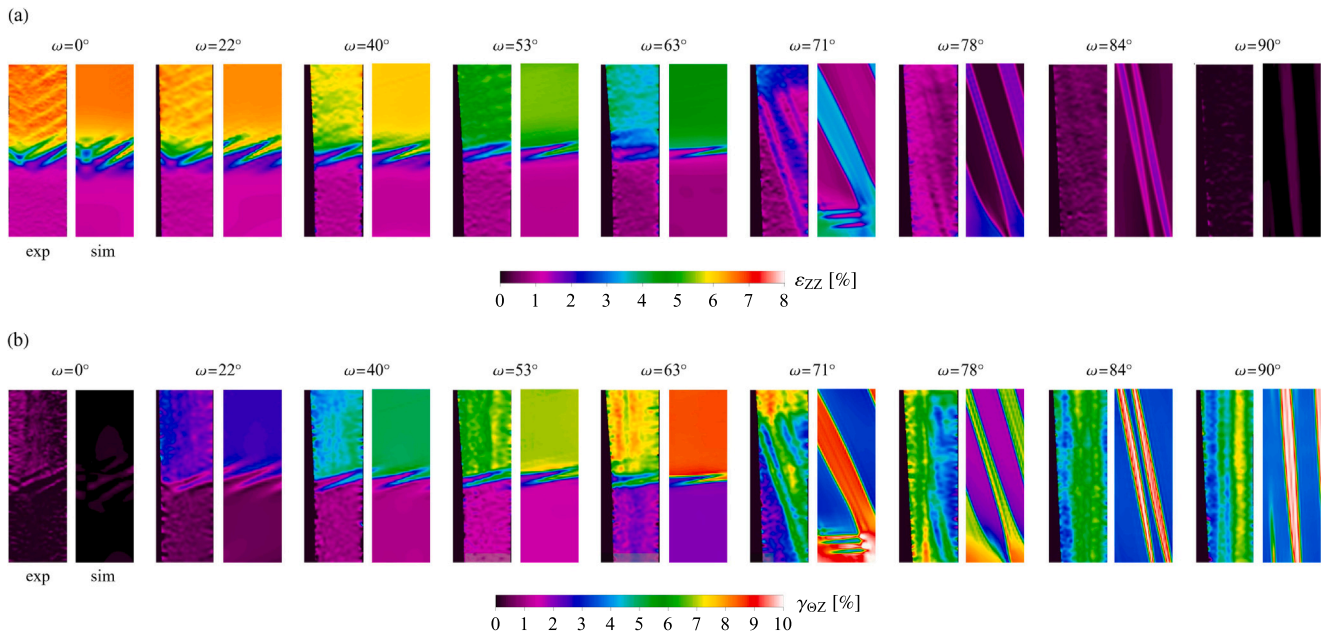

Fig. 20. Close-up views of the transformation pattern (taken in the undeformed and unwrapped-tube configuration) represented by (a) the axial strain field ε_{ZZ}, and (b) the shear strain field $\gamma_{\Theta Z}$ in combined tension–torsion. The left-hand and right-hand snapshots correspond, respectively, to the experiment (taken from Fig. 21 of Reedlunn et al. (2020a), reproduced with permission from Elsevier) and simulation. In the case of simple torsion ($\omega = 90°$), the close-up view relates to the simulation with an initial radial compression induced by the collets, see Fig. 8.

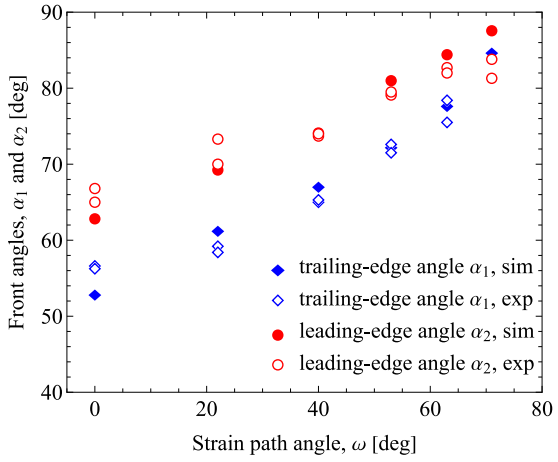

Fig. 21. Front angles α_1 and α_2 as a function of strain-path angle ω in combined tension–torsion. The angles α_1 and α_2 are measured in the undeformed and unwrapped-tube configuration.

for the case with $\omega = 71°$, the angles refer to the secondary front fingers, which are oriented almost perpendicular to the tube axis. The level of agreement is impressive, with near-coincidence observed in certain instances.

3.6. NiTi tube under combined compression–torsion

To provide a more comprehensive picture of the problem at hand and also to assess the predictive capabilities of our computational model, we expand our analysis to encompass the compression–torsion quadrant. Given the difficulties associated with the simulation of thin-walled tubes under compressive loads, primarily arising from the phenomenon of buckling, our analysis is limited to strain paths of modest compression, i.e., within the range of $96° \le \omega \le 109°$. We inferred from our supplementary analysis that the buckling instability emerges due to the simplified form of the dissipation potential (9) which neglects the dissipation associated with martensite reorientation.[3] Note that a limit friction stress of $T_c = 40$ MPa has been adopted here, as it yields results more consistent with the experiment compared to $T_c = 20$ MPa utilized in tension–torsion loading.

The results of the compression–torsion series are shown in Figs. 22–24. Prior to analyzing the results, it is worth noting that the experimental transformation patterns for this loading scenario are rather vague, and the transformation morphologies for different strain-path angles exhibit limited commonalities. It is thus particularly challenging to capture the observed diverse characteristics in our simulations. Moreover, the discrepancy between the intrinsic response of the model in compression with respect to the experimental response, see Fig. 3(b) and the related discussion in Section 3.2, further exacerbates the discrepancy between the predicted and experimental global stress–strain responses under combined compression–torsion. Nevertheless, some qualitative agreements can be pinpointed between the simulation and experimental results, although the level of agreement is not as high as in the tension–torsion loading. In what follows, we highlight the most salient observations.

The predicted transformation pattern exhibits a consistent trend for the cases analyzed. Specifically, we observe the formation of longitudinal bands during forward transformation, and the formation of domain with multi-finger fronts that subsequently shrinks into helical band during reverse transformation. As the strain path angle ω is increased, the tube exhibits a more pronounced homogeneous transformation before the emergence of the bands, the strain variation between the high-strain and low-strain regions decreases (the lowest strain variation of 3% is obtained for $\omega = 109°$), and the longitudinal bands become more inclined with respect to the tube axis. On the other hand, in the experiment, the forward and reverse transformation patterns are of the same character, both featuring longitudinal bands, where the bands are clearly visible for $\omega = 96°$ and vaguely visible for $\omega =$

[3] As a result, the internal variable $\bar{e}^t$, which describes the transformation strain of oriented martensite, can evolve freely with no energetic cost. The corresponding directional tangent stiffness is thus very low, which promotes instability.

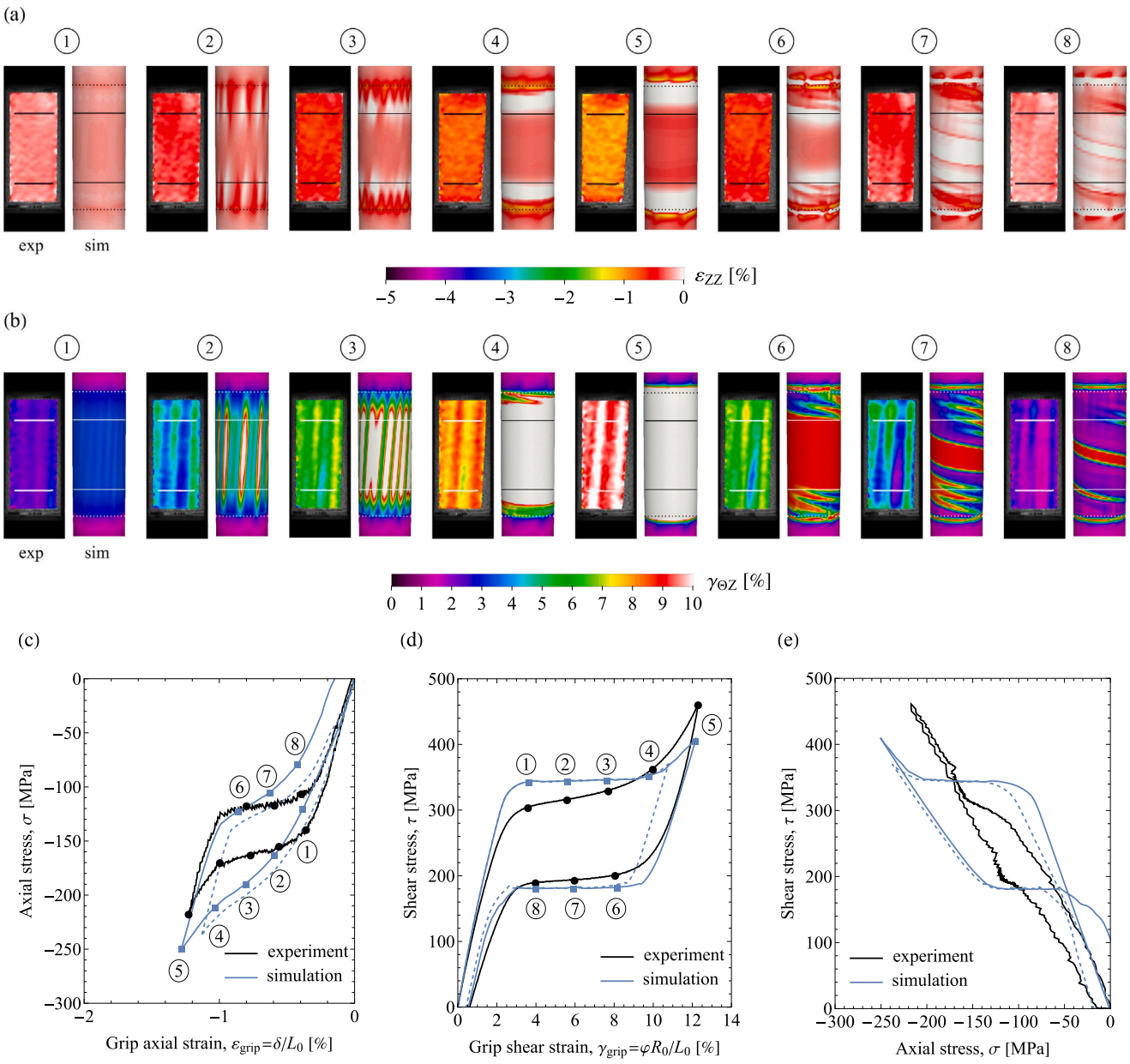

Fig. 22. Simulation results for the case of combined compression–torsion at $\omega = 96°$ and their comparison with the experimental results (case P9) of Reedlunn et al. (2020a). The left-hand and right-hand snapshots in panels (a) and (b) correspond, respectively, to the experiment (reproduced with permission from Elsevier) and simulation. The dashed curves represent the mechanical response for the case with a radial compression induced by the collet grips.

102° and 109°. In fact, the reverse transformation appears to be an inverse evolution of the forward transformation. It is worth noting that a transformation pattern characterized by multi-finger fronts has been also observed in the experiment, however, for a higher strain path angle, i.e., for the case P12 which we do not consider in this study. Another notable characteristic shared between the predicted and experimental results is the increased diffuseness of the strain fields in comparison to tension–torsion.

Concerning the mechanical responses, there exist certain aspects that are worth detailed examination and discussion. To begin with, the predicted axial responses are observed to be smooth and monotonic (during both loading and unloading), while the predicted shear responses display an apparent stress plateau and a series of abrupt (though minor) stress drops that reflect the distinctive transformation events, and thus in this sense deviate from those in the experiment. It is important to highlight that the perceived jaggedness in the experimental axial responses is most likely an experimental artifact and should not be interpreted as being related to the transformation events. Furthermore, it can be clearly seen that the magnitude of the predicted forward transformation-onset stress in the axial (shear) responses is consistently lower (higher) than that in the experiment. This systematic discrepancy is not as pronounced during unloading, and, at times, the corresponding curves demonstrate a better agreement. Recall that the maximum load in the simulation is deliberately set to a lower stress radius $\sqrt{\sigma^2+\tau^2}$ than in the experiment in order to sidestep the potential numerical issues (in terms of the poor convergence behavior of the Newton method) at high compressive loads. Nonetheless, the maximum load reached during loading may also affect the response during unloading, as detailed in Appendix B of Reedlunn et al. (2020a).

Lastly, a comparison between the predicted and experimental shear stress–axial stress (τ–σ) responses reveals substantial differences. Firstly, the experimental curves exhibit a noticeably narrower hysteresis. Secondly, the intersection of the unloading curve with that of loading is observed in all cases in the simulation, while in the experiment

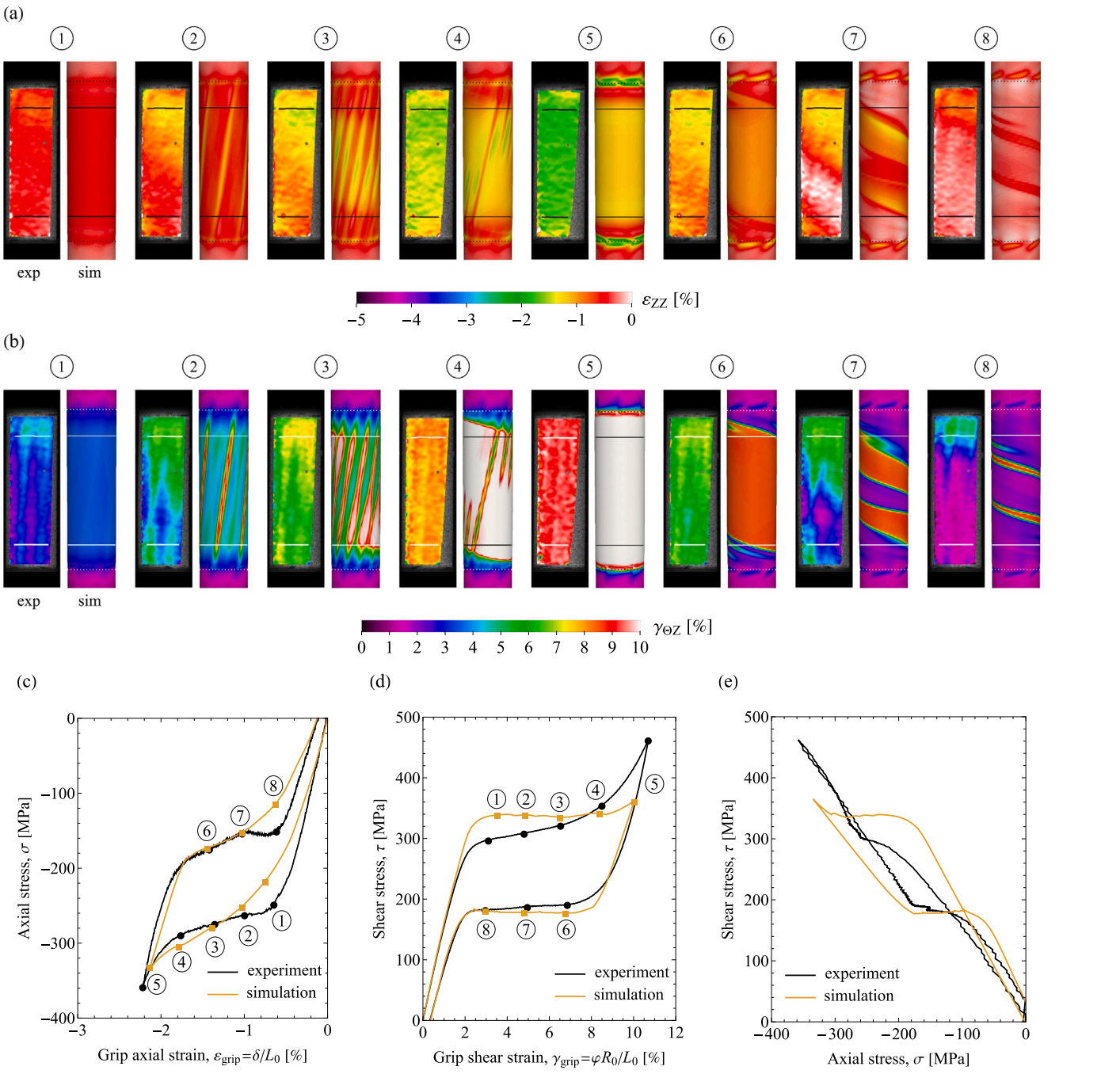

Fig. 23. Simulation results for the case of combined compression–torsion at $\omega = 102°$ and their comparison with the experimental results (case P10) of Reedlunn et al. (2020a). The left-hand and right-hand snapshots in panels (a) and (b) correspond, respectively, to the experiment (reproduced with permission from Elsevier) and simulation.

it is observed for $\omega = 102°$ and $\omega = 109°$, but not for $\omega = 96°$. The particular behavior observed for $\omega = 96°$ can be qualitatively reproduced by considering the radial compression induced by the collet (corresponding to the outer radius reduction by about 0.01 mm, as before), as shown by the dashed curve in Fig. 22(e).

Figs. 25 and 26 provide a summary of the results regarding compression–torsion loading. In contrast to the tension–torsion scenario, a clear and coherent sequence of morphological changes is not immediately discernible in the transformation patterns. This is, to some extent, because the homogeneous transformation becomes increasingly dominant as the strain-path angle ω approaches a compression-dominated state, thus hindering a clear interpretation of the localized transformation patterns. Despite this, formation of longitudinal bands is somewhat evident in both simulation and experiment, with the bands being visibly clearer in the simulation. Note that the possible buckling of the tube in the experiment has been regarded as an additional factor that further complicates the situation.

The final notable aspect is the systematic discrepancy between the experimentally-determined and simulation-based characteristic stresses, as evidenced by the markers plotted on the global τ–σ response in Fig. 25(c). Indeed, this discrepancy is not unexpected, given the discrepancies observed in the mechanical responses shown in Figs. 22–24. This aspect has been already elaborated in Section 3.5, see Fig. 19, and the potential reasons for such discrepancy have been outlined.

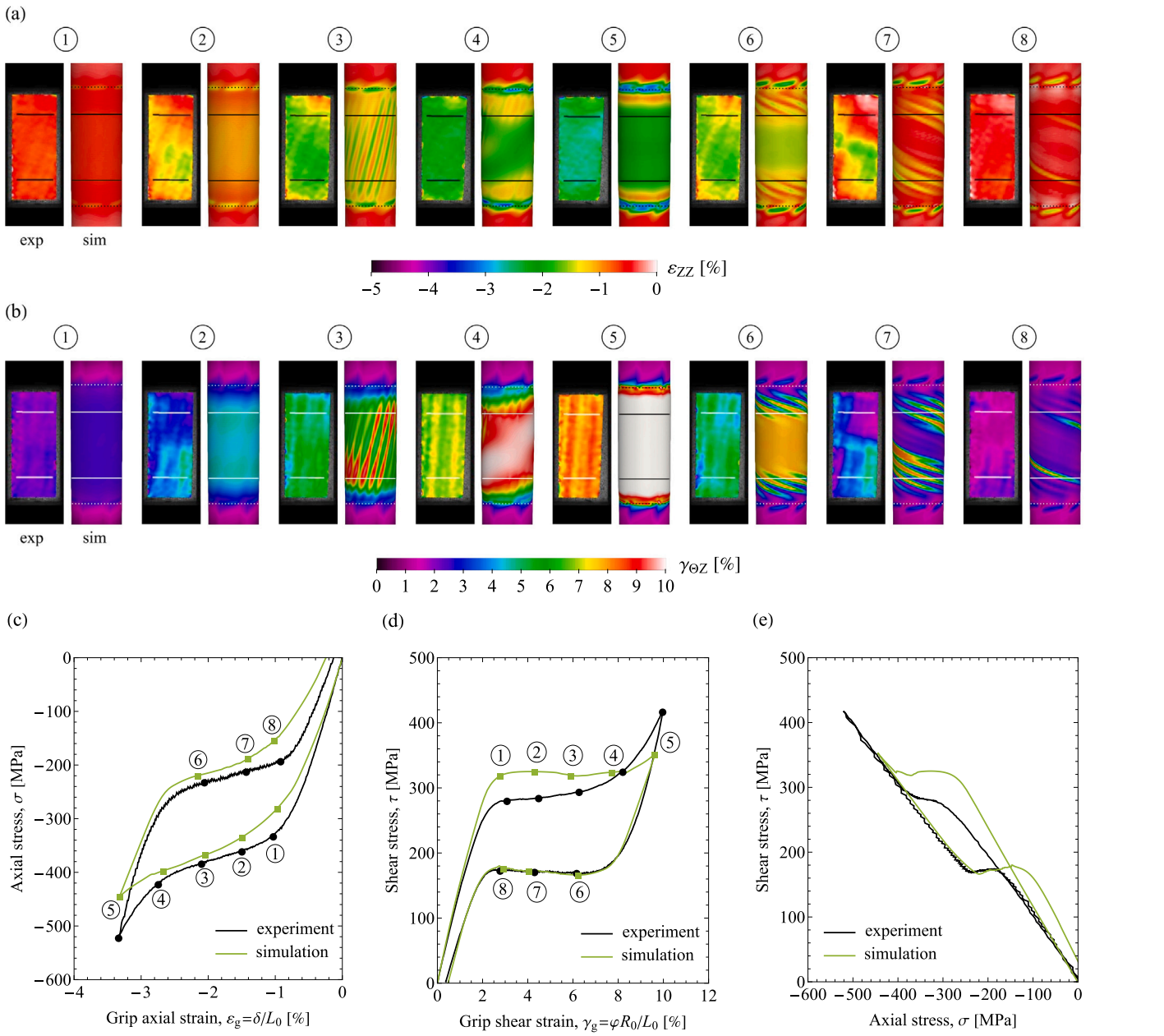

Fig. 24. Simulation results for the case of combined compression–torsion at $\omega = 109°$ and their comparison with the experimental results (case P11) of Reedlunn et al. (2020a). The left-hand and right-hand snapshots in panels (a) and (b) correspond, respectively, to the experiment (reproduced with permission from Elsevier) and simulation.

4. Conclusion

Two distinct modes of propagating instabilities have been observed in the experiment of Reedlunn et al. (2020a): the incipient helical bands and multi-finger fronts that prevail in tension-dominated tests, and the longitudinal bands that prevail in torsion-dominated tests. While the former have been thoroughly investigated in previous modeling efforts (e.g., He and Sun, 2009; Jiang et al., 2017; Rezaee-Hajidehi et al., 2020; Rezaee-Hajidehi and Stupkiewicz, 2021), the latter, unique to the experiment of Reedlunn et al. (2020a), have not been addressed so far. Motivated by this, the present study delves into the modeling of propagating instabilities in NiTi tubes subjected to proportional axial–torsion loading using a gradient-enhanced phenomenological model of pseudoelasticity. Our modeling scenario closely mimics the experiment of Reedlunn et al. (2020a) and includes several axial–twist strain paths corresponding to tension–torsion and compression–torsion loading cases.

In this study, we advocate the hypothesis attributing the emergence of longitudinal bands to the residual stresses stored in the NiTi tubes together with the non-uniformity caused by the collet grips, despite the fact that Reedlunn et al. (2020a) presented evidence and argued that the non-uniformity of the grips was not a contributing factor. To account for these effects, we have introduced the eigenstrains that induce residual stresses and have employed a simplified contact representation of the collet–tube interaction in our finite-element simulations. Our results suggest that it is the interrelated impact of both factors that give rise to longitudinal bands, albeit the predicted bands do not possess all the features of the bands observed in the experiment. Moreover, the longitudinal bands are predicted only when the intrinsic shear stress–shear strain response exhibits softening or mild hardening, while significant hardening is observed in the experiment. This means that the model does not encompass all the important factors to fully match the experiment. It should be also noted that certain model parameters adopted in the simulations, such as the softening modulus H_T and the

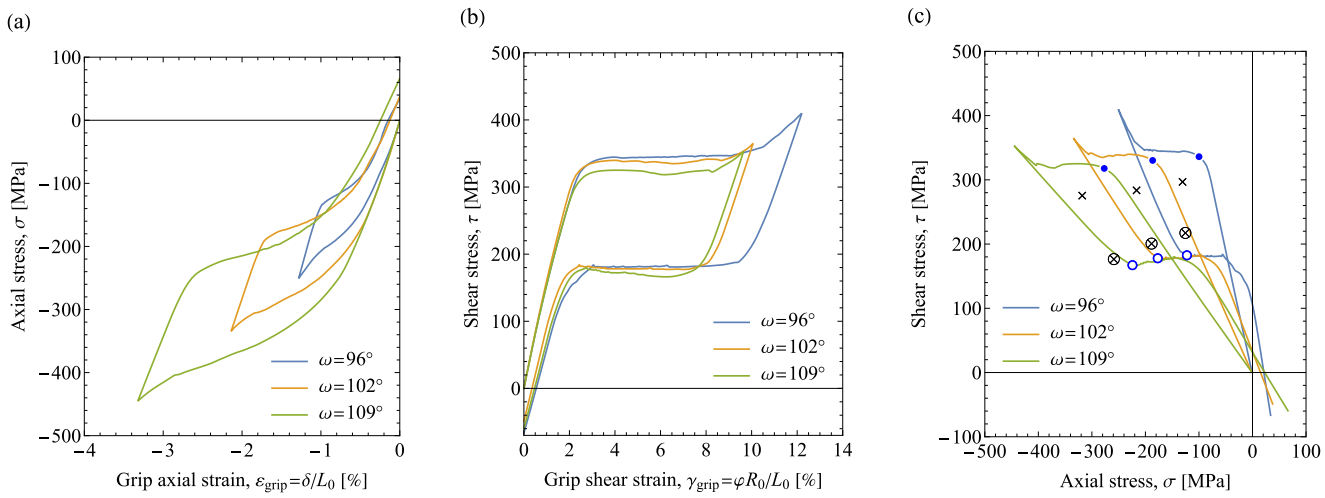

Fig. 25. Global mechanical responses in combined compression–torsion. The blue circles in panel (c) denote the characteristic transformation stresses extracted from the simulation responses, while the cross markers denote the analogous experimental points.

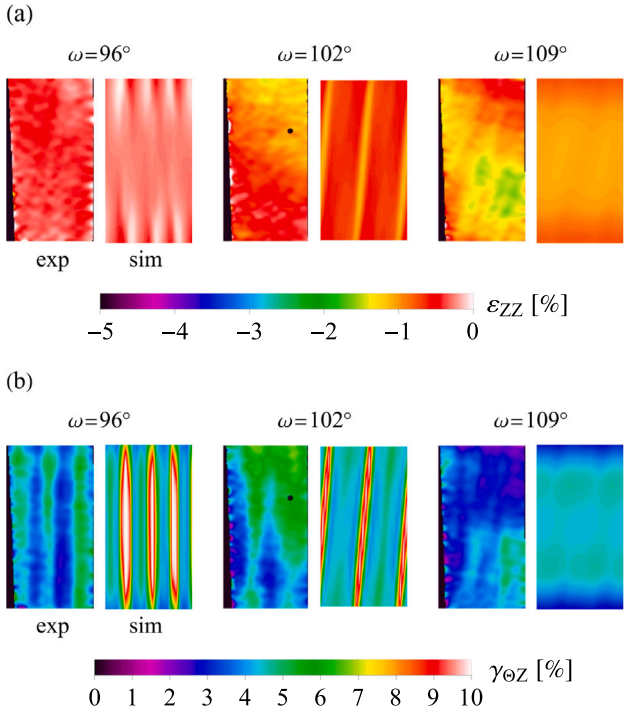

Fig. 26. Close-up views of the transformation pattern (taken in the undeformed and unwrapped-tube configuration) represented by (a) the axial strain field ε_{ZZ}, and (b) the shear strain field $\gamma_{\Theta Z}$ in combined compression–torsion. The left-hand and right-hand snapshots correspond, respectively, to the experiment (taken from Fig. 22 of Reedlunn et al. (2020a), reproduced with permission from Elsevier) and simulation.

transverse isotropy parameter β, carry a degree of uncertainty. Consequently, the obtained results and conclusions may vary depending on the specific values assigned to these parameters.

Reedlunn et al. (2020a) speculated that the inherent texture and anisotropy of NiTi tubes may contribute to the formation of longitudinal bands. Our model already takes into account this anisotropy through the transformation strain. Adjusting the austenite–martensite interaction energy to incorporate this anisotropy may also favor longitudinal bands over ring-like fronts, as suggested by Sedlák et al. (2021), see also Frost et al. (2021). Nevertheless, this hypothesis has not been investigated in the present study.

The simulation results demonstrate a successful prediction of the transformation patterns in tension-dominated paths, with an accurate characterization of the front angles that exhibit an exceptionally close agreement with the experiment. Moreover, the transition from the multi-finger fronts to longitudinal bands occurring at an intermediate strain path angle of $\omega = 71°$, along with the corresponding complex mixed-mode transformation morphology have been correctly reproduced. On the other hand, the simulation results for compression–torsion cases exhibit only some qualitative agreement with the experiment. The primary cause for this discrepancy can be traced to the simplicity of our model of pseudoelasticity and its inability to quantitatively represent the intrinsic response in compression. Additional refinements of the model would be necessary to improve the accuracy of the predictions under compressive loading conditions. Moreover, the transformation patterns developed in the compression–torsion experiments lack a consistent set of features in different strain paths, which further contributes to the challenge of capturing them with a reasonable degree of accuracy.

Furthermore, our phenomenological model of pseudoelasticity is subject to certain limitations that preclude it from reproducing some of the intricate features observed in the experiment. Notably, the simplified description of the martensite reorientation mechanism results in the model's inability to capture the striations left by the propagating fronts. This, in turn, contributes to a qualitatively different reverse transformation patterning compared to the experiment, as observed for the majority of the loading paths analyzed. A more accurate representation of the martensite reorientation mechanism would be a possible next step to improve the predictive capabilities of the model.

Declaration of competing interest

The authors declare that they have no known competing financial interests or personal relationships that could have appeared to influence the work reported in this paper.

Data availability

Data will be made available on request.

Acknowledgments

This work has been supported by the National Science Centre (NCN) in Poland through the Grant No. 2021/43/D/ST8/02555. The authors wish to thank the anonymous reviewers for their valuable remarks which greatly improved the quality of this manuscript.

Appendix A. Specification of the constitutive equations

A.1. Deformation gradient $\boldsymbol{F}^0$ associated with residual stresses

For the tubular geometry under consideration, it is justifiably assumed that the eigenstrains leading to residual stresses at each material point are described by the axial and radial volume-preserving stretches $\boldsymbol{\Lambda}_{\mathrm{R}}$ and $\boldsymbol{\Lambda}_{\mathrm{Z}}$ that take the following form in the cylindrical coordinate system,

$$\boldsymbol{\Lambda}_{\mathrm{R}} = \mathrm{diag}(\lambda_{\mathrm{R}}, 1/\sqrt{\lambda_{\mathrm{R}}}, 1/\sqrt{\lambda_{\mathrm{R}}}), \quad \boldsymbol{\Lambda}_{\mathrm{Z}} = \mathrm{diag}(1/\sqrt{\lambda_{\mathrm{Z}}}, 1/\sqrt{\lambda_{\mathrm{Z}}}, \lambda_{\mathrm{Z}}), \tag{A.1}$$

where the stretches λ_{R} and λ_{Z} are defined in terms of the strain parameters ϵ_{R} and ϵ_{Z}, respectively, and are assumed to vary linearly through the tube wall-thickness. In particular, $\lambda_{\mathrm{R}} = 1 + \epsilon_{\mathrm{R}}$ on the tube outer surface, $\lambda_{\mathrm{R}} = 1 - \epsilon_{\mathrm{R}}$ on the tube inner surface, and $\lambda_{\mathrm{R}} = 1$ at the tube mid-thickness (and like-wise for λ_{Z}). On account of the axial symmetry of the problem, the sole radial coordinate of the material point determines its eigenstrains. Since the eigenstrains are assumed isochoric, an arbitrary volume-preserving stretch $\boldsymbol{\Lambda} = \boldsymbol{\Lambda}_{\mathrm{R}}\boldsymbol{\Lambda}_{\mathrm{Z}}$ (of diagonal representation in the cylindrical coordinate system) can be uniquely specified by adequately prescribing λ_{R} and λ_{Z} (thorough ϵ_{R} and ϵ_{Z}). Accordingly, there is no need to introduce an independent hoop counterpart of $\boldsymbol{\Lambda}_{\mathrm{R}}$ and $\boldsymbol{\Lambda}_{\mathrm{Z}}$.

The deformation gradient $\boldsymbol{F}^0$ is then formulated as

$$\boldsymbol{F}^0 = \boldsymbol{Q}\boldsymbol{\Lambda}_{\mathrm{R}}\boldsymbol{\Lambda}_{\mathrm{Z}}\boldsymbol{Q}^{\mathrm{T}}, \tag{A.2}$$

where the rotation tensor $\boldsymbol{Q}$ (a rotation about the tube axis) is required to transform the stretch tensors $\boldsymbol{\Lambda}_{\mathrm{R}}$ and $\boldsymbol{\Lambda}_{\mathrm{Z}}$ from the cylindrical coordinate system to the global Cartesian coordinate system. Upon applying the deformation gradient $\boldsymbol{F}^0$ at each material point, the corresponding incompatible deformation results in the buildup of residual stresses. Clearly, the deformation gradient $\boldsymbol{F}^0$ preserves the volume, i.e., $\det \boldsymbol{F}^0 = 1$.

We refer to the experiment of Reedlunn et al. (2020a) in order to determine the eigenstrain parameters ϵ_{R} and ϵ_{Z}. They reported that quarter-ring specimens cut from their NiTi tubes bent radially inward, and the measured radius of the curvature was 740 ± 100 mm. Our finite-element computations, carried out for the same quarter-ring configuration, have shown that the desired curvature can be obtained, for instance, by setting $\epsilon_{\mathrm{R}} = 0$ and $\epsilon_{\mathrm{Z}} = 0.08\%$. Similarly, the same curvature can be achieved by setting $\epsilon_{\mathrm{R}} = -0.15\%$ and $\epsilon_{\mathrm{Z}} = 0$. It thus follows that the eigenstrains and residual stresses cannot be uniquely determined solely based on fitting the curvature of the quarter-ring specimen. In fact, if one of the eigenstrain components (ϵ_{R} or ϵ_{Z}) is prescribed arbitrarily, the other can be adjusted such that it yields the desired curvature.

Subsequently, we investigated the effect of the residual stresses induced by the eigenstrains on the formation of longitudinal bands under simple torsion (as discussed in Section 3.4). It turned out that the longitudinal bands do not form for the two cases discussed above, in view of the insufficient magnitude of the resulting residual stresses. Consequently, alternative combinations of ϵ_{R} and ϵ_{Z} were explored in search of a combination that would yield the desired curvature and, at the same time, would promote the longitudinal bands under torsion. Through this analysis, the combination of $\epsilon_{\mathrm{R}} = -1\%$ and $\epsilon_{\mathrm{Z}} = -0.45\%$ were identified that satisfy both conditions. Accordingly, these values have been adopted in our main simulations. As mentioned above, this choice is not unique, but no other indications exist to guide a more definitive identification of ϵ_{R} and ϵ_{Z}.

A.2. The Helmholtz free energy components

The chemical energy ϕ_0 is defined as the weighted sum of the free energy density (in a stress-free state) of pure austenite phase ϕ_0^{a} and that of pure martensite phase ϕ_0^{m},

$$\phi_0(\eta) = (1-\eta)\phi_0^{\mathrm{a}} + \eta\phi_0^{\mathrm{m}} = \phi_0^{\mathrm{a}} + \Delta\phi_0\eta, \tag{A.3}$$

where $\Delta\phi_0 = \phi_0^{\mathrm{m}} - \phi_0^{\mathrm{a}}$ is called the chemical energy of phase transformation. As the present model is limited to pseudoelasticity, $\Delta\phi_0$ is selected such that austenite is stable in stress-free conditions, that is to say $\Delta\phi_0 > 0$.

An isotropic elastic strain energy is considered in the following neo-Hookean form,

$$\phi_{\mathrm{el}}(\boldsymbol{F}, \bar{\boldsymbol{e}}^{\mathrm{t}}, \eta) = \frac{1}{2}\mu(\eta)(\mathrm{tr}\,\hat{\boldsymbol{b}}^{\mathrm{e}} - 3) + \frac{1}{4}\kappa(\det \boldsymbol{b}^{\mathrm{e}} - 1 - \log(\det \boldsymbol{b}^{\mathrm{e}})), \tag{A.4}$$

where, in view of Eqs. (1)–(3), $\boldsymbol{b}^{\mathrm{e}} = \boldsymbol{F}^{\mathrm{e}}(\boldsymbol{F}^{\mathrm{e}})^{\mathrm{T}} = \boldsymbol{F}(\boldsymbol{F}^0)^{-1}\exp(-2\eta\bar{\boldsymbol{e}}^{\mathrm{t}})(\boldsymbol{F}^0)^{-\mathrm{T}}\boldsymbol{F}^{\mathrm{T}}$ is the left Cauchy–Green tensor, and $\hat{\boldsymbol{b}}^{\mathrm{e}} = (\det \boldsymbol{b}^{\mathrm{e}})^{-1/3}\boldsymbol{b}^{\mathrm{e}}$ is its isochoric part. As it is commonly assumed, the shear modulus μ varies during the phase transformation and is obtained by applying the Reuss mixing rule to the shear moduli of pure austenite and martensite phases, i.e., $1/\mu(\eta) = (1-\eta)/\mu_{\mathrm{a}} + \eta/\mu_{\mathrm{m}}$, whereas the bulk modulus κ remains constant, i.e., $\kappa = \kappa_{\mathrm{a}} = \kappa_{\mathrm{m}}$ (e.g., Sedlak et al., 2012; Auricchio et al., 2014). Note that intriguing observations from experimental studies, including Reedlunn et al. (2020a), indicate that the apparent elastic modulus of martensite after transformation under compression is visibly higher than that under tension, see also Thomasová et al. (2017). This feature is neglected in our model and the elastic moduli in our simulations are adopted with reference to the apparent elastic response of the material in tension, see the discussion below.

Some additional considerations have been taken into account in selecting the elastic moduli of austenite and martensite phases in our simulations. Firstly, our model assumes isotropic elasticity (rather than transversely isotropic elasticity which would be physically more relevant for drawn tubes) and does not incorporate additional inelastic mechanisms such as the intermediate R-phase transformation and detwinning. Accordingly, the shear moduli in our simulations are adjusted so that the resulting more compliant elastic response approximates the effects that are not explicitly included in our model, and thereby, the adopted elastic moduli differ somewhat from those measured and reported by Reedlunn et al. (2020a), see Table E.1.

Finally, the gradient energy ϕ_{grad} is formulated as a quadratic function of the gradient of the martensite volume fraction η in the reference configuration,

$$\phi_{\mathrm{grad}}(\nabla\eta) = \frac{1}{2}G\nabla\eta\cdot\nabla\eta, \tag{A.5}$$

where G is a positive parameter that governs the energy associated with the diffuse austenite–martensite interfaces (macroscopic transformation fronts). It can be shown, through the analytical solution of the one-dimensional small-strain version of the model, that the nominal thickness of such a diffuse interface is determined as $\lambda = \pi\sqrt{-G/H}$, provided that the term $h(\eta)$ is absent in Eq. (11) and the constant interaction energy coefficient H is negative, i.e., for a softening-type trilinear intrinsic response (Rezaee-Hajidehi and Stupkiewicz, 2018).

Appendix B. Micromorphic regularization

A micromorphic regularization of the present gradient-enhanced model is formulated in the spirit of Forest (2009). Within the present framework, the micromorphic approach is regarded as a means to facilitate the finite-element implementation of the model. The general idea of the micromorphic approach is presented in Forest (2009), and the details of the numerical implementation can be found in Rezaee-Hajidehi and Stupkiewicz (2018), see also Mazière and Forest (2015).

The micromorphic regularization is based on the introduction of a new global degree of freedom $\breve{\eta}$. The variable $\breve{\eta}$ is linked to the martensite volume fraction η through a quadratic penalization term ϕ_{pen} which is added into the Helmholtz free energy function ϕ, Eq. (8), and takes the form

$$\phi_{\mathrm{pen}}(\eta, \breve{\eta}) = \frac{1}{2}\chi(\eta - \breve{\eta})^2. \tag{B.1}$$

The penalty parameter χ is adopted such that a sufficiently small discrepancy between $\breve{\eta}$ and η is ensured. Next, the gradient energy ϕ_{grad}, Eq. (A.5), is reformulated in terms of the gradient of the micromorphic variable $\breve{\eta}$, i.e., $\phi_{\text{grad}}(\nabla\breve{\eta}) = 1/2\, G\nabla\breve{\eta}\cdot\nabla\breve{\eta}$, so that the Helmholtz free energy takes the form

$$\phi(\boldsymbol{F},\bar{\boldsymbol{e}}^{\text{t}},\eta,\breve{\eta},\nabla\breve{\eta}) = \phi_0(\eta)+\phi_{\text{el}}(\boldsymbol{F},\bar{\boldsymbol{e}}^{\text{t}},\eta)+\phi_{\text{int}}(\bar{\boldsymbol{e}}^{\text{t}},\eta)+\phi_{\text{grad}}(\nabla\breve{\eta})+\phi_{\text{pen}}(\eta,\breve{\eta}). \tag{B.2}$$

Upon this treatment, the volume fraction η is transformed to a local quantity and the corresponding evolution equation can be solved at the local level (i.e., at the Gauss points in the finite-element setting), which in turn enables a simpler treatment of the complexities associated with its constitutive relations.

On the other hand, the micromorphic variable $\breve{\eta}$ is a global unknown that is governed by a Helmholtz-type PDE,

$$\breve{\eta} - \ell^2\nabla^2\breve{\eta} = \eta, \quad \ell = \sqrt{\frac{G}{\chi}}, \tag{B.3}$$

with ℓ as the corresponding length-scale parameter. Note that Eq. (B.3) results naturally from the micromorphic formulation (i.e., it is not postulated).

Appendix C. Thermomechanically coupled model

In the proportional loading program considered in this paper, the loading rates are relatively low and correspond to nearly isothermal conditions (Reedlunn et al., 2020a). Thereby, the temperature gradient is practically negligible during the phase transformation. Nevertheless, the computations are performed using the thermomechanically-coupled model. This provides a natural regularization to the problem, and thereby, significantly improves the robustness of the model at the instants of abrupt events, such as nucleation and annihilation of interfaces. Here, the formulation is presented briefly. For a more detailed presentation, the reader is referred to Rezaee-Hajidehi et al. (2020).

First, the effect of temperature on the mechanical response is accounted for by incorporating the temperature dependence of the chemical energy ϕ_0. Upon assuming an identical specific heat capacity for the austenite and martensite phases, i.e., $c^{\text{a}} = c^{\text{m}} = c$, a linear relation is established between the temperature T and the chemical energy of transformation, $\Delta\phi_0$, so that we have

$$\phi_0(\eta,T) = \phi_0^{\text{a}}(T) + \Delta\phi_0(T)\eta, \quad \Delta\phi_0(T) = \Delta s^*(T-T_{\text{t}}), \tag{C.1}$$

where $\Delta s^* = s_0^{\text{a}} - s_0^{\text{m}}$ denotes the entropy difference between pure austenite and martensite phases, T_{t} denotes the thermodynamic equilibrium temperature, and the free energy of pure austenite phase in a stress-free reference state has the usual form, $\phi_0^{\text{a}}(T) = u_0^{\text{a}} - s_0^{\text{a}}T + \varrho_0 c\left(T - T_0 - T\log\left(T/T_0\right)\right)$, with u_0^{a}, s_0^{a}, $\varrho_0 c$, and T_0 denoting, respectively, the internal energy, entropy, specific heat capacity, and reference temperature.

Next, heat conduction and related temperature changes are included in the model. The internal heat source $\dot{R}$ is formulated to represent the latent heat of transformation and the heat release due to mechanical dissipation,

$$\dot{R} = \Delta s^* T\dot{\eta} + f_{\text{c}}|\dot{\eta}|. \tag{C.2}$$

Assuming a thermally isotropic material, the Fourier's law of heat conduction is expressed as (Holzapfel, 2006)

$$\varrho_0 c\dot{T} + \nabla\cdot\boldsymbol{Q} = \dot{R}, \quad \boldsymbol{Q} = -K\boldsymbol{C}^{-1}\nabla T, \tag{C.3}$$

where $\boldsymbol{Q}$ is the Piola–Kirchhoff (nominal) heat flux, K is the heat conduction coefficient, and $\boldsymbol{C} = \boldsymbol{F}^{\text{T}}\boldsymbol{F}$ is the right Cauchy–Green strain tensor. The Piola–Kirchhoff heat flux $\boldsymbol{Q}$ is related to the Cauchy (spatial) heat flux $\boldsymbol{q}$ via the Piola transformation, $\boldsymbol{Q} = J\boldsymbol{F}^{-1}\boldsymbol{q}$, where $J = \det\boldsymbol{F}$. The heat conduction Eq. (C.3) is accompanied by the standard boundary conditions.

Appendix D. Finite-element implementation

In this appendix, we highlight the most important aspects related to the computer implementation of the model. For more details, see Rezaee-Hajidehi et al. (2020).

In view of the non-differentiability of the rate-independent dissipation ΔD at $\Delta\eta = 0$, Eq. (9), the minimization problem for η (to be solved at the local level thanks to the micromorphic regularization) is non-smooth, and thus not amenable to a straightforward finite-element implementation. To resolve this issue, following Stupkiewicz and Petryk (2013), the augmented Lagrangian technique is employed that handles simultaneously both the non-differentiability of ΔD and the inequality constraint on the martensite volume fraction, $0 \le \eta \le 1$, and thus transforms the local non-smooth problem in terms of η to an equivalent smooth saddle-point problem in terms of η and the adjoint Lagrange multiplier. The model also involves an equality constraint $g(\bar{\boldsymbol{e}}^{\text{t}}) = 0$ associated with the transformation strain $\bar{\boldsymbol{e}}^{\text{t}}$, cf. Eq. $(4)_2$, that is handled by employing standard Lagrange multiplier technique. For brevity, the respective computational details are not described here.

As discussed in Section 3.1, the load in the simulations is applied through the frictional interaction between the tube surface and the rigid surfaces of the collet grips, and a Tresca-type frictional contact model is utilized for this purpose. The contact model is implemented in the finite-element framework by means of the penalty regularization technique (e.g., Lengiewicz et al., 2011). In practical terms, the penalty regularization admits a certain degree of violation of the contact conditions (namely the bilateral contact conditions and the limit friction condition). In particular, an elastic tangential displacement between the two surfaces is allowed. Nevertheless, the associated penalty parameter is selected such that the violation is adequately small and, meanwhile, the computational performance is not adversely affected. Note that in some special cases, it is assumed that the collet grips induce a constant radial compression to the tube. Accordingly, to properly account for the compression effects, the steel dowel pins inside the tube (Reedlunn et al., 2020a) are also modeled, as rigid surfaces with frictionless (bilateral) contact interaction.

The complete thermomechanically-coupled model involves three global unknown fields, namely the displacement $\boldsymbol{u} = \boldsymbol{\varphi} - \boldsymbol{X}$, the micromorphic variable $\breve{\eta}$ and the temperature T. 20-noded quadratic hexahedral elements (with serendipity shape functions and reduced $2\times2\times2$ integration rule) are used for the displacement field $\boldsymbol{u}$, whereas 8-noded linear hexahedral elements are used for $\breve{\eta}$ and T. The nonlinear system of equations obtained by the finite-element discretization are solved monolithically by means of the Newton method. The symbolic code generation *Mathematica* toolbox *AceGen* (Korelc, 2009; Korelc and Wriggers, 2016) is employed to generate the finite-element codes. As a result, by taking advantage of the automatic differentiation (AD) technique available in *AceGen*, the tangent matrix required in the Newton method is computed by exact linearization, and hence guarantees the quadratic convergence of the Newton method. The generated finite-element codes are then used in the *Mathematica* toolbox *AceFEM* (Korelc and Wriggers, 2016) to run the finite-element simulations.

In all the simulations, the free length of the tube, see Fig. 2(a), is discretized by a uniform mesh with the element size of 0.125 mm within the tube surface (which corresponds to 80 elements along the circumference), while through the thickness, to avoid unnecessary excessive computational cost, the element size of 0.318 mm is used (i.e., one element through the thickness). At the same time, a non-uniform mesh is adopted within the gripped parts of the tube, with the mesh getting gradually coarser towards the tube ends. By and large, depending on the total length of the tube (free length and the gripped parts), the problem size ranges between 600 000 and 1 200 000 degrees of freedom. Note that the finite-element size has been chosen based on a preliminary mesh-sensitivity analysis and our prior experience

Table E.1
Model parameters used in the simulations.

Parameter		Value	Remark
κ	Bulk modulus	130 GPa	Within the typical range of bulk modulus for NiTi.
μ_a	Shear modulus for austenite phase	16.5 GPa	Calibrated with reference to the uniaxial tensile response of NiTi tube in the experiment of Reedlunn et al. (2020a).
μ_m	Shear modulus for martensite phase	10.5 GPa	(see above)
T_t	Equilibrium temperature	215 K	(see above)
f_c	Hysteresis loop parameter	6 MPa	(see above)
ϵ_T	Maximum tensile transformation strain	5%	(see above)
H_T	Softening modulus in tension	−5 MPa	(see above and the discussion in Section 3.2)
α	Tension–compression asymmetry ratio	1.4	Selected with reference to the uniaxial compressive response of NiTi tube in the experiment of Reedlunn et al. (2020a), see the discussion in Section 3.2.
H_C	Hardening modulus in compression	8 MPa	(see above)
β	Transverse isotropy parameter	1.3	Yields the desired intrinsic response in shear.
$\boldsymbol{m}$	Axis of transverse isotropy	$(0, 0, 1)$	Along the tube axis.
Δs^*	Chemical energy of transformation	0.24 MPa/K	Taken from our previous studies (Rezaee-Hajidehi and Stupkiewicz, 2018; Rezaee-Hajidehi et al., 2020).
K	Heat conductivity coefficient	18 W/(m K)	(see above)
ρc_0	Specific heat	2.86 MJ/(m^3 K)	(see above)
G	Gradient energy parameter	10 Pa mm^2	Selected based on prior modeling experiences.
χ	Micromorphic penalty parameter	500 MPa	Ensures that $\check{\eta}$ is reasonably close to η.
a_1	Nonlinear hardening parameter	5 MPa	Introduces an adequate nonlinearity to the intrinsic responses.
a_2	Nonlinear hardening parameter	0.46	(see above)
a_3	Nonlinear hardening parameter	11	(see above)
ϵ_R	Parameter specifying residual stresses	−1%	Determined based on experimental data of Reedlunn et al. (2020a), see Appendix A.1.
ϵ_Z	Parameter specifying residual stresses	−0.45%	(see above)

such that the mesh is adequately fine to effectively resolve the diffuse austenite–martensite interfaces and to represent the subtle features of the complex transformation patterns. For a detailed discussion on the effect of mesh density on the simulation results, we refer the interested reader to our previous study (Rezaee-Hajidehi et al., 2020).

Appendix E. Material parameters

All the material parameters adopted in the finite-element simulations are described in Table E.1, unless stated otherwise. Note that the parameter T_c, which defines the limit friction stress at the collet grips, is not included in Table E.1, as its value varies in different simulations depending on the loading combination analyzed, see the related discussion in the respective sections.

Appendix F. Mechanical responses in terms of average strains

In Fig. F.1, we showcase representative σ–$\bar{\epsilon}_{ZZ}$ and τ–$\bar{\gamma}_{\Theta Z}$ responses for both tension–torsion and compression–torsion loading scenarios. By excluding the grip effects, we obtain a more accurate representation of the true global mechanical responses. It is notable that in the particular case of $\omega = 22°$, the σ–$\bar{\epsilon}_{ZZ}$ and τ–$\bar{\gamma}_{\Theta Z}$ responses exhibit a better agreement with experimental data than the responses based on the grip strains, compare Fig. 11(c,d) and Fig. F.1(a). In other cases, also those not included in Fig. F.1, the agreement with the experiment is similar for both representations.

References

Abeyaratne, R., Knowles, J.K., 1993. A continuum model of a thermoelastic solid capable of undergoing phase transitions. J. Mech. Phys. Solids 41, 541–571.

Alarcon, E., Heller, L., Arbab Chirani, S., Šittner, P., Kopeček, J., Saint-Sulpice, L., Calloch, S., 2017. Fatigue performance of superelastic NiTi near stress-induced martensitic transformation. Int. J. Fatigue 95, 76–89.

Auricchio, F., Bonetti, E., Scalet, G., Ubertini, F., 2014. Theoretical and numerical modeling of shape memory alloys accounting for multiple phase transformations and martensite reorientation. Int. J. Plast. 59, 30–54.

Bechle, N.J., Kyriakides, S., 2014. Localization in NiTi tubes under bending. Int. J. Solids Struct. 51, 967–980.

Bechle, N.J., Kyriakides, S., 2016. Evolution of localization in pseudoelastic NiTi tubes under biaxial stress states. Int. J. Plast. 82, 1–31.

Bhattacharya, K., 1992. Self-accommodation in martensite. Arch. Ration. Mech. Anal. 120, 201–244.

Churchill, C.B., Shaw, J.A., Iadicola, M.A., 2009. Tips and tricks for characterizing shape memory alloy wire: Part 3—Localization and propagation phenomena. Exp. Tech. 33, 70–78.

Daly, S., Ravichandran, G., Bhattacharya, K., 2007. Stress-induced martensitic phase transformation in thin sheets of Nitinol. Acta Mater. 55, 3593–3600.

Ericksen, J.L., 1975. Equilibrium of bars, vol. 5. pp. 191–201.

Feng, P., Sun, Q.P., 2006. Experimental investigation on macroscopic domain formation and evolution in polycrystalline NiTi microtubing under mechanical force. J. Mech. Phys. Solids 54, 1568–1603.

Feng, P., Sun, Q.P., 2007. In situ profilometry for non-uniform strain field measurement of NiTi shape memory alloy microtubing under complex stress states. Smart Mater. Struct. 16, S179.

Forest, S., 2009. Micromorphic approach for gradient elasticity, viscoplasticity, and damage. J. Eng. Mech. 135 (3), 117–131.

Frost, M., Benešová, B., Seiner, H., Kružík, M., Šittner, P., Sedlák, P., 2021. Thermomechanical model for NiTi-based shape memory alloys covering macroscopic localization of martensitic transformation. Int. J. Solids Struct. 221, 117–129.

Greenly, J.L., Kyriakides, S., Tsimpoukis, S., 2023. On the underlying material response of pseudoelastic NiTi. Eur. J. Mech. A Solids 105023.

Hallai, J.F., Kyriakides, S., 2013. Underlying material response for Lüders-like instabilities. Int. J. Plast. 47, 1–12.

He, Y.J., Sun, Q.P., 2009. Effects of structural and material length scales on stress-induced martensite macro-domain patterns in tube configurations. Int. J. Solids Struct. 46, 3045–3060.

He, Y.J., Sun, Q.P., 2010. Rate-dependent domain spacing in a stretched NiTi strip. Int. J. Solids Struct. 47, 2775–2783.

Holzapfel, G.A., 2006. Nonlinear Solid Mechanics. Wiley, Chichester.

Jiang, D., Kyriakides, S., Landis, C.M., 2017. Propagation of phase transformation fronts in pseudoelastic NiTi tubes under uniaxial tension. Extreme Mech. Lett. 15, 113–121.

Kelly, A., Stebner, A.P., Bhattacharya, K., 2016. A micromechanics-inspired constitutive model for shape-memory alloys that accounts for initiation and saturation of phase transformation. J. Mech. Phys. Solids 97, 197–224.

Korelc, J., 2009. Automation of primal and sensitivity analysis of transient coupled problems. Comput. Mech. 44, 631–649.

Korelc, J., Wriggers, P., 2016. Automation of Finite Element Methods. Springer International Publishing, Switzerland.

Lagoudas, D., Hartl, D., Chemisky, Y., Machado, L., Popov, P., 2012. Constitutive model for the numerical analysis of phase transformation in polycrystalline shape memory alloys. Int. J. Plast. 32, 155–183.

Lengiewicz, J., Korelc, J., Stupkiewicz, S., 2011. Automation of finite element formulations for large deformation contact problems. Internat. J. Numer. Methods Engrg. 85, 1252–1279.

Li, Z.Q., Sun, Q.P., 2002. The initiation and growth of macroscopic martensite band in nano-grained NiTi microtube under tension. Int. J. Plast. 18, 1481–1498.

Mazière, M., Forest, S., 2015. Strain gradient plasticity modeling and finite element simulation of Lüders band formation and propagation. Contin. Mech. Thermodyn. 27, 83–104.

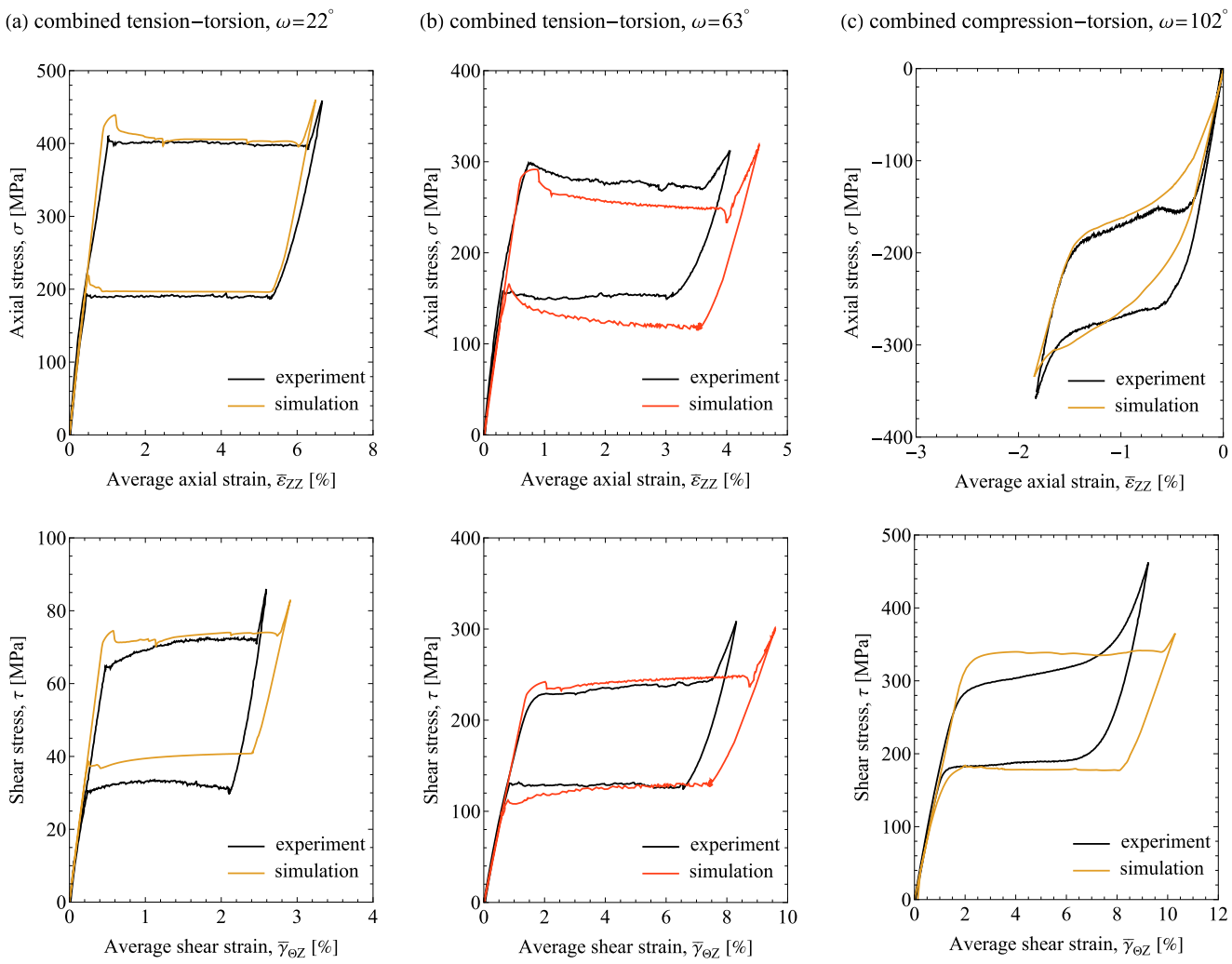

Fig. F.1. Selected mechanical responses in terms of the average strains $\bar{\varepsilon}_{ZZ}$ and $\bar{\gamma}_{\Theta Z}$ and their comparison with the experimental results of Reedlunn et al. (2020a): (a) tension–torsion with $\omega = 22°$ (case P1), (b) tension–torsion with $\omega = 63°$ (case P4), and (c) compression–torsion with $\omega = 102°$ (case P10).

Miyazaki, S., Imai, T., Otsuka, K., Suzuki, Y., 1981a. Lüders-like deformation observed in the transformation pseudoelasticity of a Ti–Ni alloy. Scripta Metall. 15, 853–856.

Miyazaki, S., Otsuka, K., Suzuki, Y., 1981b. Transformation pseudoelasticity and deformation behavior in a Ti-50.6 at% Ni alloy. Scripta Metall. 15, 287–292.

Orgéas, L., Favier, D., 1998. Stress-induced martensitic transformation of a NiTi alloy in isothermal shear, tension and compression. Acta Mater. 46, 5579–5591.

Petryk, H., 2003. Incremental energy minimization in dissipative solids. C.R. Mecanique 331, 469–474.

Peultier, B., Ben Zineb, T., Patoor, E., 2006. Macroscopic constitutive law of shape memory alloy thermomechanical behaviour. Application to structure computation by FEM. Mech. Mat. 38, 510–524.

Reedlunn, B., Churchill, C.B., Nelson, E.E., Shaw, J.A., Daly, S.H., 2014. Tension, compression, and bending of superelastic shape memory alloy tubes. J. Mech. Phys. Solids 63, 506–537.

Reedlunn, B., LePage, W.S., Daly, S.H., Shaw, J.A., 2020a. Axial-torsion behavior of superelastic tubes: Part I, proportional isothermal experiments. Int. J. Solids Struct. 199, 1–35.

Reedlunn, B., LePage, W.S., Daly, S.H., Shaw, J.A., 2020b. Raw data, supplemental plots, and videos for 'Axial-torsion behavior of superelastic tubes: Part i, proportional isothermal experiments'. http://dx.doi.org/10.17632/rsfg5474tr.1.

Rezaee-Hajidehi, M., Stupkiewicz, S., 2018. Gradient-enhanced model and its micromorphic regularization for simulation of Lüders-like bands in shape memory alloys. Int. J. Solids Struct. 135, 208–218.

Rezaee-Hajidehi, M., Stupkiewicz, S., 2021. Modelling of propagating instabilities in pseudoelastic NiTi tubes under combined tension–torsion: helical bands and apparent yield locus. Int. J. Solids Struct. 221, 130–149.

Rezaee-Hajidehi, M., Tůma, K., Stupkiewicz, S., 2020. Gradient-enhanced thermomechanical 3D model for simulation of transformation patterns in pseudoelastic shape memory alloys. Int. J. Plast. 128, 102589.

Sadjadpour, A., Bhattacharya, K., 2007. A micromechanics-inspired constitutive model for shape-memory alloys. Smart Mater. Struct. 16 (5), 1751.

Safaei, K., Nematollahi, M., Bayati, P., Kordizadeh, F., Taheri Andani, M., Abedi, H., Poorganji, B., Elahinia, M., 2022. On the crystallographic texture and torsional behavior of NiTi shape memory alloy processed by laser powder bed fusion: Effect of build orientation. Addit. Manuf. 59, 103184.

Sedlak, P., Frost, M., Benešová, B., Zineb, T.B., Šittner, P., 2012. Thermomechanical model for NiTi-based shape memory alloys including R-phase and material anisotropy under multi-axial loadings. Int. J. Plast. 39, 132–151.

Sedlák, P., Frost, M., Ševčík, M., Seiner, H., 2021. 3D spatial reconstruction of macroscopic austenite–martensite transition zones in NiTi wires induced by tension and twisting using diffraction/scattering computed tomography. Int. J. Solids Struct. 228, 111122.

Shariat, B.S., Li, Y., Yang, H., Wang, Y., Liu, Y., 2022. Shear strain evolution during tension-induced Lüders-type deformation of polycrystalline NiTi plates. Mater. Sci. Eng. A 839, 142774.

Shaw, J.A., Kyriakides, S., 1995. Thermomechanical aspects of NiTi. J. Mech. Phys. Solids 43, 1243–1281.

Shaw, J.A., Kyriakides, S., 1997a. Initiation and propagation of localized deformation in elasto-plastic strips under uniaxial tension. Int. J. Plast. 13, 837–871.

Shaw, J.A., Kyriakides, S., 1997b. On the nucleation and propagation of phase transformation fronts in a NiTi alloy. Acta Mater. 45, 683–700.

Stupkiewicz, S., Petryk, H., 2010. A bi-crystal aggregate model of pseudoelastic behaviour of shape-memory alloy polycrystals. Int. J. Mech. Sci. 52 (2), 219–228.

Stupkiewicz, S., Petryk, H., 2013. A robust model of pseudoelasticity in shape memory alloys. Internat. J. Numer. Methods Engrg. 93, 747–769.

Stupkiewicz, S., Rezaee-Hajidehi, M., Petryk, H., 2021. Multiscale analysis of the effect of interfacial energy on non-monotonic stress–strain response in shape memory alloys. Int. J. Solids Struct. 221, 77–91.

Sun, Q.-P., Li, Z.-Q., 2002. Phase transformation in superelastic NiTi polycrystalline micro-tubes under tension and torsion—from localization to homogeneous deformation. Int. J. Solids Struct. 39, 3797–3809.

Thamburaja, P., Anand, L., 2001. Polycrystalline shape-memory materials: effect of crystallographic texture. J. Mech. Phys. Solids 49 (4), 709–737.

Thomasová, M., Seiner, H., Sedlák, P., Frost, M., Ševčík, M., Szurman, I., Kocich, R., Drahokoupil, J., Šittner, P., Landa, M., 2017. Evolution of macroscopic elastic moduli of martensitic polycrystalline NiTi and NiTiCu shape memory alloys with pseudoplastic straining. Acta Mater. 123, 146–156.

Wang, J., Moumni, Z., Zhang, W., 2017. A thermomechanically coupled finite-strain constitutive model for cyclic pseudoelasticity of polycrystalline shape memory alloys. Int. J. Plast. 97, 194–221.

Watkins, R.T., Reedlunn, B., Daly, S., Shaw, J.A., 2018. Uniaxial, pure bending, and column buckling experiments on superelastic NiTi rods and tubes. Int. J. Solids Struct. 146, 1–28.

Zhao, Z., Jiang, D., Xiao, Y., Lin, J., Min, J., 2023. Intrinsic response of nanocrystalline superelastic NiTi shape memory alloy. Extreme Mech. Lett. 60, 101988.